

An Interoperable Multi-Objective Batch Bayesian Optimization Framework for High-Throughput Materials Discovery

Trevor Hastings¹, Mrinalini Mulukutla¹, Danial Khatamsaz¹, Daniel Salas¹, Wenle Xu¹, Daniel Lewis¹, Nicole Person¹, Matthew Skokan¹, Braden Miller¹, James Paramore¹, Brady Butler^{1,2}, Douglas Allaire³, Ibrahim Karaman¹, George Pharr¹, Ankit Srivastava¹, and Raymundo Arroyave¹

1: *Texas A&M University College Station, Department of Materials Science and Engineering, College Station TX, 77843, USA*

2: *DEVCOM Army Research Laboratory South at Texas A&M University, College Station, TX, 77843, USA*

3: *Texas A&M University College Station, Department of Mechanical Engineering, College Station TX, 77843, USA*

Abstract

In this study, we introduce a groundbreaking framework for materials discovery, we efficiently navigate a vast phase space of material compositions by leveraging Batch Bayesian statistics in order to achieve specific performance objectives. This approach addresses the challenge of identifying optimal materials from an untenably large array of possibilities in a reasonable timeframe with high confidence. Crucially, our batchwise methods align seamlessly with existing material processing infrastructure for synthesizing and characterizing materials. By applying this framework to a specific high entropy alloy system, we demonstrate its versatility and robustness in optimizing properties like strain hardening, hardness, and strain rate sensitivity. The Bayesian model's adeptness in refining and expanding the property Pareto front highlights its broad applicability across various materials, including steels, shape memory alloys, ceramics, and composites. This study advances the field of materials science and sets a new benchmark for material discovery methodologies. By proving the effectiveness of Bayesian optimization, we showcase its potential to redefine the landscape of materials discovery.

Main Text

Materials discovery methods have long been a pillar of Materials Science. The process of employing a technique to optimize this discovery remains an area of active research. Engineering applications are accurately represented by multi-objective optimization problems, as one cannot reasonably maximize a single material property, such as tensile strength, at the cost of all others. Furthermore, typical fabrication and characterization techniques are designed to manage several specimens in tandem; there is therefore a disconnect between the many sequential optimization strategies in literature and the physical expectations of industrialists. Many authors have used machine learning (ML) models to guide optimization strategies, including support vector machines, random forests, and active learning approaches, but only managing to do so with 1 objective^{1, 2, 3, 4, 5}. Multi-objective ML techniques have been demonstrated but without experimental validation; it is unclear what optimization in batches would entail beyond simply manufacturing the best predicted candidate^{6, 7, 8}. Even in the case of batch ML experimental works, candidates have been based off of existing literature alone⁹. Of these, there is a lack of Bayesian techniques, despite it being excellently suited to handle black box structure-property problems¹⁰. There are few optimization frameworks to date that are both Bayesian and multi-objective: one additive manufacturing example was limited to pre-existing material inputs that were known to be manufacturable, and the framework began with random sampling¹¹. Overall, optimization techniques in literature either limit themselves to a single objective, materials based on existing literature, or sequential experiments, making them ill-suited as materials discovery methods that industry can utilize, like one would use for modern ballistics applications. Batch Bayesian optimization, expandable to any number of objectives, is demonstrated in this work as an ideal framework for material discovery.

The efficacy of a multi-objective optimization problem can be evaluated by the progression in its data point values that most accomplish the overall objective—e.g., maximizing several material properties at once. In practice, there is no material with perfect property values. If one wants to increase strength, there will be a point where it comes at the cost of ductility. This means that with the definition of two or more goals, there will be a set of “best” materials. For example, suppose two materials “M1” and “M2” with ultimate tensile strength (UTS) and Young’s modulus (E) of $M1 = \{UTS: 900 \text{ (MPa)}, E: 200 \text{ (GPa)}\}$ and $M2 = \{UTS: 800 \text{ (MPa)}, E: 220 \text{ (GPa)}\}$. Both of these would be objectively better than a third material “M3” with worse properties in every aspect: $M3 = \{UTS: 600 \text{ (MPa)}, E: 150 \text{ (GPa)}\}$. “M3” would be considered to have a poor combination of inputs by comparison to produce this result (atomic fractions, heat treatments, molecular weights, etc.). However, M1 and M2 cannot be called “better” or “worse” than each other without additional application-relevant restrictions; there is merely a tradeoff of one desirable property for another. These points are said to have *Pareto efficiency*, and compose the *Pareto front* for the dataset. This concept is illustrated in [Fig. 1](#). A mathematical definition of Pareto efficiency can be found in [Supplementary Information](#).

Maximal Pareto Efficiency

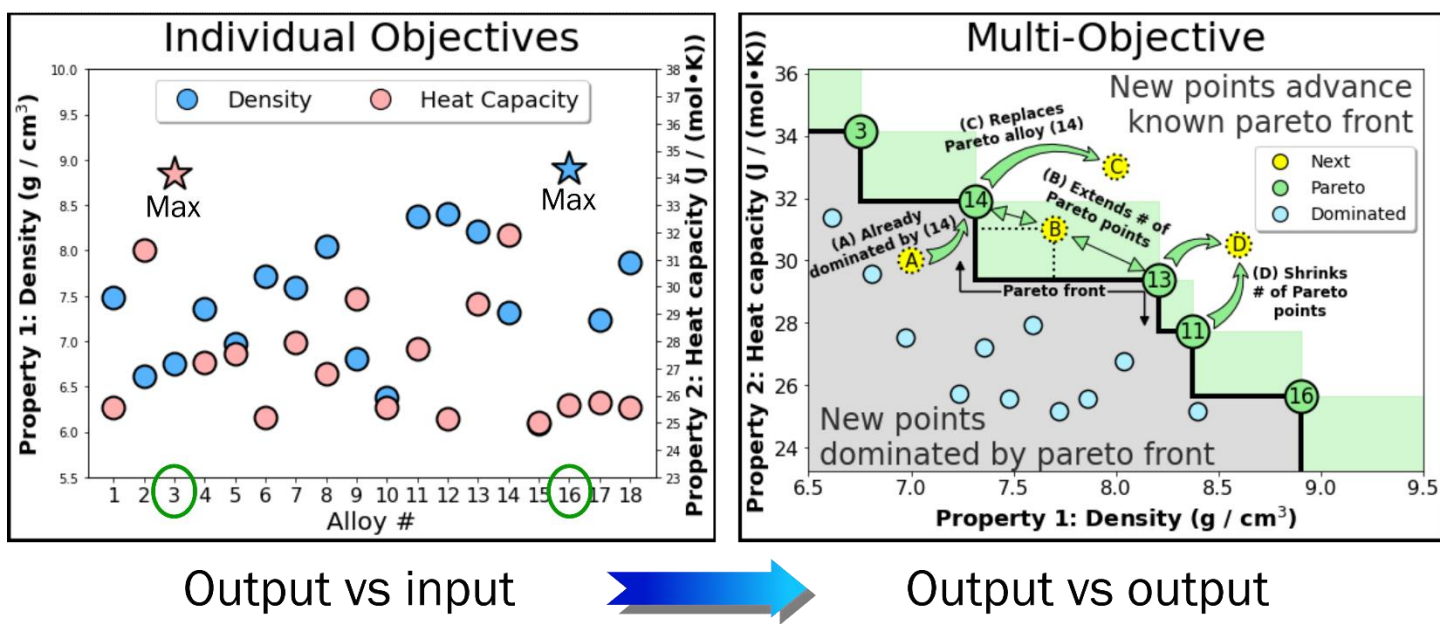


Figure 1: Visualization of the Pareto front for a multi-objective optimization problem, where the objectives are maximized. When analyzing objectives individually, the best respective data point is simply the one with the maximum value. When objectives are considered equally important, an array of “best possible” data points emerges where one objective is traded for another.

The maximization of individual objectives ([Fig. 1 left](#)) only produces a single maximum value in practice: alloy #3 for heat capacity or alloy #16 for density. When a maximum is demanded of two objectives at once, it becomes unclear by tracking single objectives alone which data points best meet this criteria. By simultaneously comparing objectives ([Fig. 1 right](#)), a set of possible data points comprising the Pareto set will satisfy this goal. The alloys with extreme cases—#3 and #16, which maximize one objective at the cost of the other—are seen on the edges of the Pareto front and are joined by other alloys that continue this property tradeoff. Unlike the single objective case where every data point will either become the new maximum or fail to do so (as a duplicate maximum is unlikely), there are 4 meaningful cases: (A) new data points (in the gray region) will already be outclassed, or *dominated*, by at least one point on the pareto set; (B) new data points (in the green region) will lie on the Pareto front and extend the number of *nondominated* data points that meet the project criteria; (C) a new data point (in the white region) will replace an existing pareto point, the analog of finding a new maximum in the single objective case; or (D), a new data point (far enough out in the white region) that is particularly successful will dominate

multiple previous pareto points. The gray region is known as the *hypervolume* (this nomenclature is common in literature, representing the fact that multi-objective problems often extend beyond three dimensions). Each newfound Pareto point will increase the value of this hypervolume, making it a viable metric for optimization progress.

“Optimization” in this context refers to the minimization of resources—time, raw materials, working hours—that it takes to find the best materials, given any number of objectives over a specific set of possible candidates. Suppose the goal is to maximize 2 objectives, and there are 1,000 possible candidates to pick from, a handful of which have been tested already. An example set of 1,000 candidates is shown in [Fig. 2 left](#), 980 of which are dominated by 20 pareto points. This is the ontological point of view, or the ground truth, as seen if one were omniscient. In the epistemological view, one only knows the properties of materials that have been tested. It can be easy to imagine struggling to find the best alloys without committing to testing nearly 1,000 materials. The usage of *Bayesian* statistics turns this untenable problem into a feasible experimental campaign: existing data points—even ones with terrible properties!—yield suggestions in the direction of the true pareto front, despite it being unknown. [Fig. 2 right](#) shows an example multi-objective Bayesian optimization that begins with the properties of 20 known materials: it finds 10 out of the 20 true Pareto points after 5 optimizations (6 iterations), or a total of 120 tested data points, a feat that random sampling would have taken ~500 tests to accomplish.

Bayesian Optimization

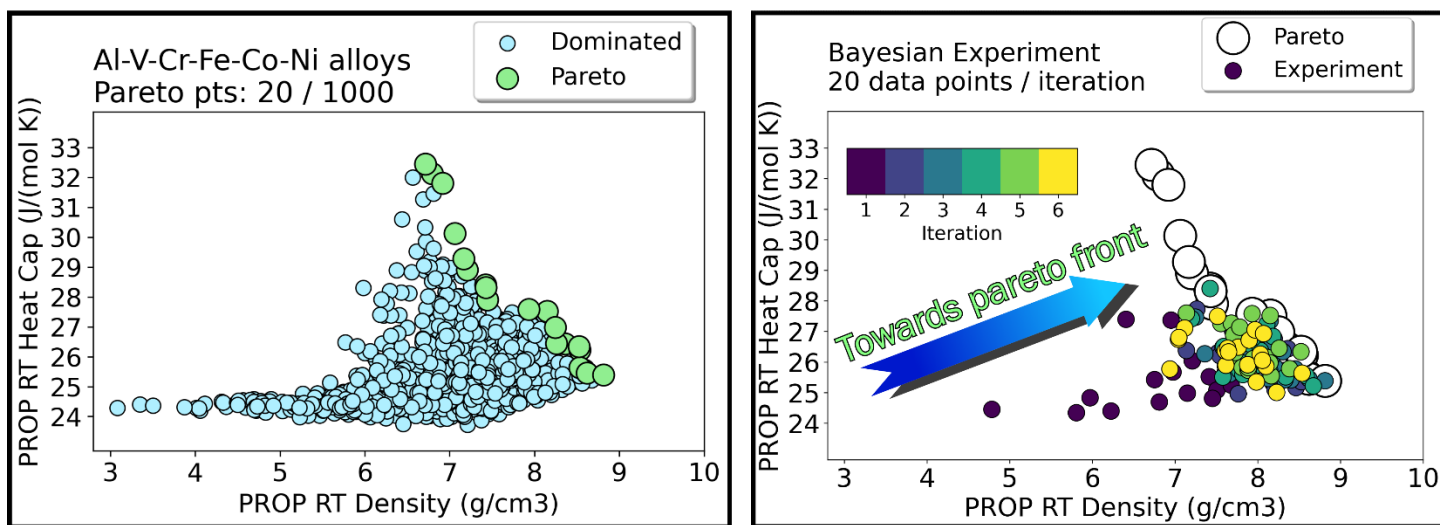


Figure 2: Example optimization experiment (right) for a given property space (left). The properties of 1,000 candidates are shown; in this case there are 20 ground truth Pareto points. After testing some initial alloys, Bayesian statistics determines the most promising materials to test in each iteration. Bayesian optimization immediately proceeds to suggest candidates closer to the true pareto front despite it being unknown.

This process, *Bayesian optimization*—emulating real world experiments by doing so in batches of materials at a time—is known as *Batch Bayesian Optimization* (BBO). It is important to note that the very nature of Bayesian optimization yields new data points in the *direction* of the pareto front, as seen in [Fig. 2 right](#). Notably, while ground truth Pareto points are often a metric used for a success in simulations (the green data points in [Fig. 2 left](#), circled in black in [Fig. 2 right](#)), whether or not these are precisely discovered is irrelevant, as materials with excellent properties will be discovered during the iterative experimental campaign. This matches the typical desire in industry to want to have flexibility over inputs (e.g. composition). The Bayesian process yields an array of decent materials near the nondominated designs, unlike a random process that would have consistently tested “bad” materials. In this work, the use of BBO allowed for the discovery of a never before seen set of nondominated materials across 3 objectives in an arbitrary material space: the Al-V-Cr-Fe-Co-Ni High Entropy Alloy (HEA) system. It is likely that the alloys listed in this work are the best in their class, and this framework can be extended to other material systems, including non-metal ones, with any industrial objectives in mind.

Any optimization campaign requires clear design objectives at the onset. Feasible materials that can be suggested as candidates via optimization need to be defined, along with methods for material synthesis, microstructural verification, characterization tools for objectives, and optimization scripts. This material system—Al-V-Cr-Fe-Co-Ni and all of its possible subsystems from 2 to 6 elements—was chosen based off of the highly studied Cr-Fe-Co-Ni system, with Al added for stacking fault energy (SFE) control and V added based on V-Co-Ni ternary alloys with incredibly high ultimate tensile strengths^{12, 13}. It was delineated at a resolution of 5 atomic %, yielding an elemental *phase space* consisting of 53,124 compositions—a rigorous method to calculate this number for any system is detailed in the [Supplementary Information](#), and code is available for doing so on this project’s GitHub repository.

To accurately predict phase stability of the alloys, we used ThermoCalc, a CALculation of PHase Diagram (CALPHAD) method. Modern CALPHAD methods have been able to achieve accurate single phase solid solution predictions for HEAs with the consideration of higher order mixing parameters to great success^{14, 15, 16, 17, 18, 19, 20, 21, 22, 23, 24, 25, 26, 27}. ThermoCalc’s TCHEA v5.1 database was used to determine which compositions would have a Face-Centered Cubic (FCC) crystal structure at 700 (°C). It was further used to calculate material properties of solidification range, density, and thermal conductivity. By judiciously constraining the system with desired material phases and properties, we reduced an untestable number of compositions to an approachable optimization problem.

Additional constraints were applied for those modeled properties: A solidification range < 100 (K) to ensure homogenization, a room temperature density < 8.5 (g/cm³) and a thermal conductivity > 5 (W/(mK)) for lightweight ballistics applications, reducing the list to 2,437 candidates. Out of the 2,437 constrained alloys, 2 experiments in parallel were initiated for this framework based on their predicted stacking fault energies (SFE), breaking up the alloys into groups with potentially different deformation mechanisms. These SFE values were calculated with a machine learning model trained on DFT data²⁸ (details included in [Supplementary Information](#)), consisting of 1,550 alloys with “low” predicted SFE < 50 (mJ/m²) and 887 alloys with “high” predicted SFE > 50 mJ/m².

A potential pitfall at the design phase would be to select a set of starting materials that are too similar to one another, or to select data points randomly, inducing luck into the optimization process. Rather than doing this by eye (alloy #1 has high Fe content, alloy #2 has high Ni content, etc.), an algorithm called *K-Medoids clustering* provides a systematic starting point. If you were to take the average of all Ni compositions across the dataset, the number would likely be some real number that does not conveniently match any one of the candidates. Medoid clustering solves this issue by dividing the data up into a number of families of similar data points, or desired clusters, and then finding the most central *data point within that cluster* (via a nearest-neighbor algorithm). This guarantees that the experiment systematically begins with a variety of starting materials. Each low and high SFE experiment selected 8 starting candidates by means of K-Medoids clustering, yielding a wide spread of starting compositions²⁹.

[Fig. 3](#) illustrates the alloys in a flattened compositional space, where alloys consisting of a primary element are closer to their labeled vertices (details of these dimensionality reduction techniques are listed in [Supplementary Information](#)).

Candidate Selection

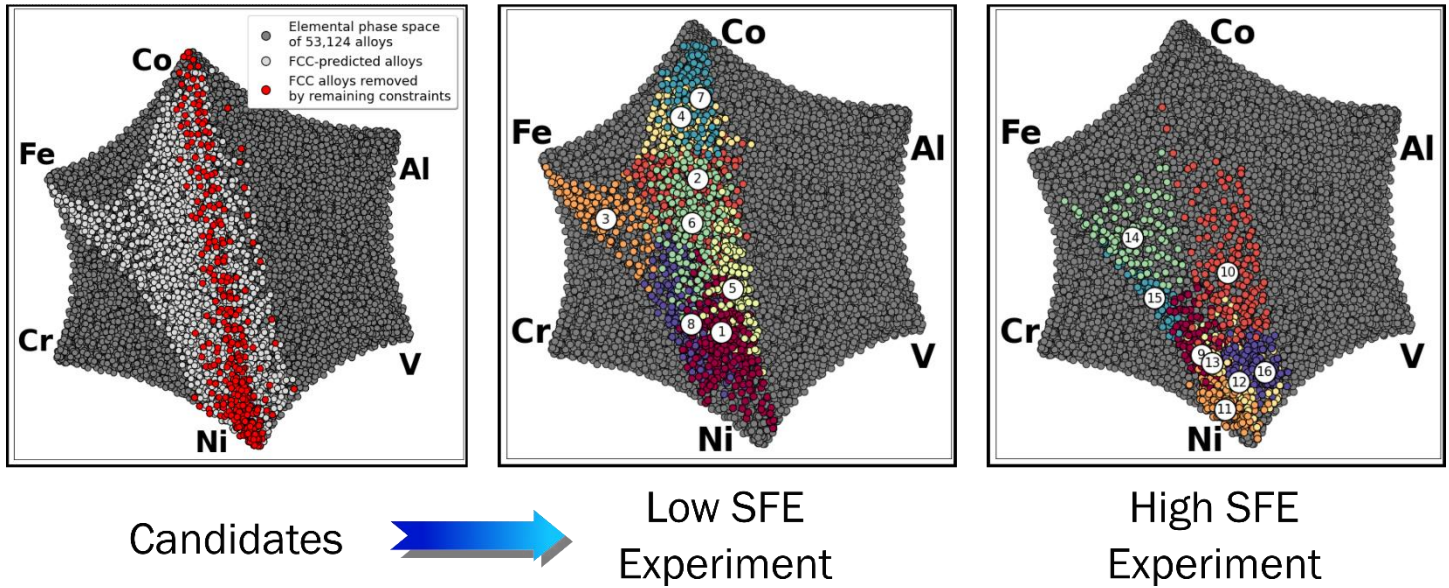


Figure 3: The initial conditions for each of the two experiments in parallel as defined by the BBO framework. (left) The elemental phase space, compositions that are predicted to be FCC, and compositions additionally removed by constraints. (middle, right) The two parallel experiments and their starting alloys. Colors correspond to medoid clusters; each number is a starting alloy guaranteed to have significantly different elemental inputs from any other medoid.

With the materials clearly defined for optimization, any number of objectives can be defined for an experimental campaign. To illustrate this framework, 3 objectives were chosen to be maximized with BBO. A summary schematic of the above techniques is shown in Fig 4 along with all of the experimental apparatuses used in this work.

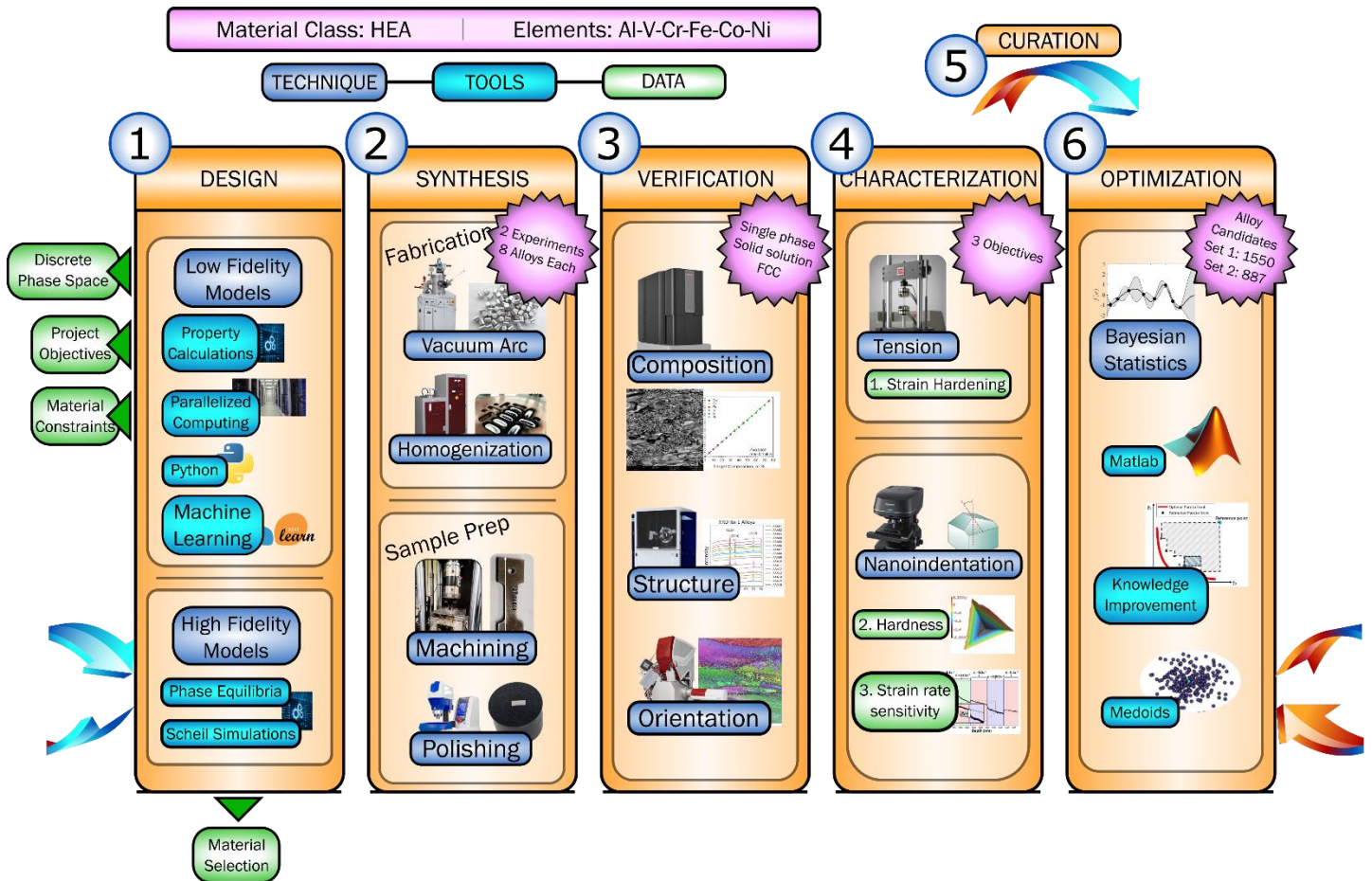


Figure 4: Schematic of a BBO framework, tailored to experimentally discover new HEAs.

Three experimental objectives were identified with potential for ballistics applications: strain hardening, hardness, and strain rate sensitivity. Strain hardening was determined from miniature tension tests, while nanoindentation was used to measure both hardness and strain rate sensitivity over strain rates of several orders of magnitude. Each of the synthesis and characterization techniques shown in Fig. 3 are detailed in Methods. Compositions for all alloys discovered in this work, phase information, and example micrographs can be found in Supplementary Information. The goal of the framework was then to maximize each of the 3 objectives, testing batches of 8 materials for each iteration, for both the low SFE and high SFE experiments in parallel. This continued until a stopping criteria was reached via BBO. There is a distinct method by which one would set up a Bayesian algorithm, which follows.

BO utilizes Bayesian statistics to evaluate black box functions for a phase space with some input—in this case, a metal alloy—in order to query a set of attributes (the 3 mechanical property values measured in this work). This algorithm attempts to maximize the hypervolume (referenced in Fig. 1) gained by each data point that *could* be tested from the space of available candidates (the 1550 in the low SFE experiment and the 887 in the high SFE experiment, minus the initial batch). It does this with a few ingredients: a function that can mathematically evaluate this hypervolume, a set of parameters that can best describe the black-box relation between inputs and outputs, and some mathematical wrapper to hold all of this information in the context of experimental data. The function used to determine hypervolume, an *acquisition function*, is known as *expected hypervolume improvement* (EHVI); it is a closed form function based off of the Normal distribution, and it has been proven successful in other environments^{30, 31, 32}. The random parameters that instantiate the model are known as *length scales*, one for each input (the atomic fractions in this work). For example, a Ni length scale of 0.05 would indicate that changing Ni by any amount is significant, whereas a length scale of 0.7 would indicate that Ni has to change considerably in order to meaningfully affect the output. We inherently do not know what the case is for each of the 6 elements, so 1,000 random sets of numbers are generated as options to potentially describe the system. We also have to provide a length scale

for each output *individually*, as changing Ni by 5 at.% might significantly affect hardness but not meaningfully change strain rate sensitivity. The “wrapper” that holds the experimental data, the experimental error, the length scales, and other necessary parameters in order to calculate EHVI is known as a *Gaussian process* (GP), a probability distribution that describes our beliefs of how the inputs relate to a given output. Each output is evaluated non-preferentially, so there are 1,000 GPs for each of the 3 objectives. EHVI is then calculated for all the untested data points using these GPs. The maximum EHVI is determined for each set of length scale options. Many of these length scale combinations will produce exactly the same suggestion, so this process yields a comparatively small (<100) number of unique candidates. There are many fine-tunings within this algorithm that go beyond the scope of this work (growth rate, choice of kernel functions, choice of differing acquisition functions, choice of batch sizes, to name a few), but any Bayesian method will need these 3 things to operate. Specific parameter values for this project are listed in [Methods](#), and example Bayesian code for this project is located on our GitHub.

The same K-medoid process of selecting disparate candidates was used to determine the 8 alloys for the next iteration of both experiments from the list of candidates produced by the BO algorithm (thus, making it a BBO algorithm). [Fig. 5 left](#) shows a simple example of this process in action with a 1D input in X (as opposed to the 6D elemental composition input in this work) with a 1D output in Y (as opposed to the 3D property output in this work). It evaluates a simple growing sinusoidal function. After a few observations determined by maximizing EHVI, the maximum of the function is reached.

Optimizing Hypervolume

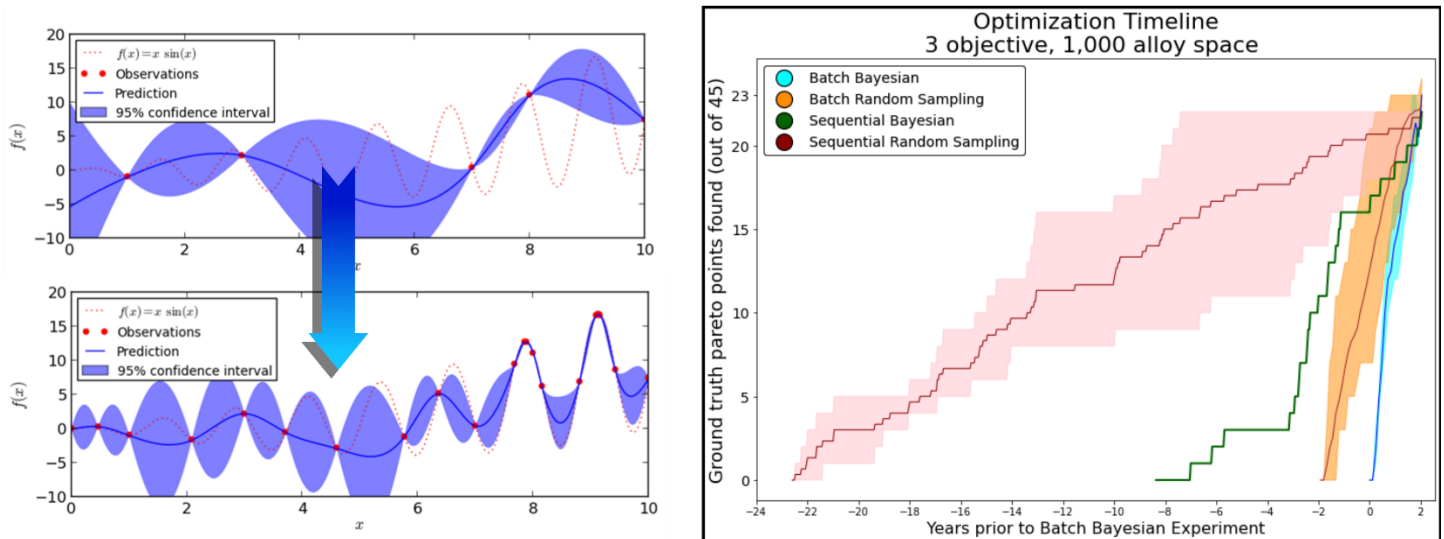


Figure 5: (left) The concept of optimizing hypervolume for a sinusoidal function. After a few predictions, the maximum is found. (right) The use of expected hypervolume improvement with real time estimates across different experiment types, all competing for the same goal within the same material space. Batch experiments test 20 data points per iteration over 6 weeks. Sequential experiments test 1 data point per iteration over 2 weeks. A year is approximated to 50 weeks. Average lines are shown between regions of the same type of experiment. Each of the experiments have been shifted such that they end at the same time as the worst BBO experiment.

[Fig. 5 \(left\)](#) illustrates the concept of the process being Bayesian: the underlying function is both tested in regions of large uncertainty—e.g. the domain between the values 3 and 7—and also regions where our prior belief suggests better candidates should exist based on the underlying function—e.g. the domain between 7 and 10. Thus, even alloys with terrible properties assist in finding better ones.

This process is *strikingly* efficient. [Fig. 5 right](#) illustrates a real-world time estimate for these types of experiments. The framework in this work was performed over periods of 6 weeks for each iteration. Due to the nature of setting up experiments, it’s estimated that performing the same framework to completion one alloy at a time—sequentially—would

take 2 weeks per iteration. Suppose you were to take an example dataset with 1,000 candidates and start two experiments to find half of the ground truth pareto points, testing alloys one at a time, one random experiment and one Bayesian experiment. In order to finish the experiments at the same time, you would have had to begin the random sequential experiment over 10 years earlier! The batch case is a truncated version of this: random sampling takes multiple extra years to finish even for a small dataset. [Fig. 5 right](#) also shows the importance of batch selection over that of sequential. At a reasonable synthesis rate of 20 samples per iteration over 3x the time, any batch method used is producing materials at ~7x the rate. Thus, any sequential method used—Bayesian or otherwise—would have to be 7x as effective just to compete with batch experiments chosen with random selections.

Five iterations were enough to illustrate a meaningful level of convergence towards the pareto set in this design space. [Fig. 6 top](#) shows the final 80 alloys discovered by the optimization framework used in this study. 3D Pareto property surfaces of the iterations can be found in [Supplementary Information](#).

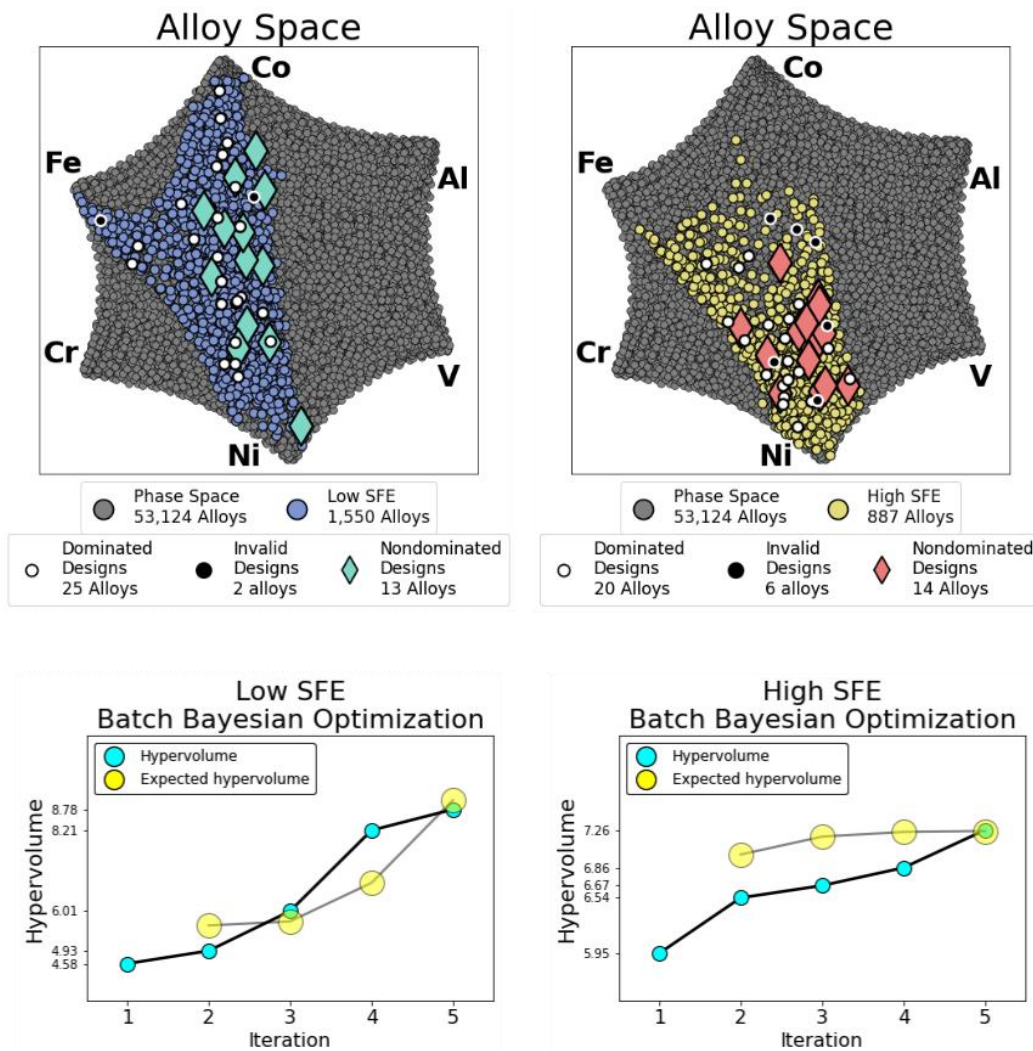


Figure 6: (top) The pareto (nondominated) sets for each BBO experiment. Designs that did not meet project constraints despite predictions are in black, and were not included in optimization. (bottom) Hypervolumes of the data at each iteration, and hypervolumes predicted by data from the previous iteration using EHVI.

While it is impossible say definitively that a black-box function's Pareto front has been found, one can still show progression of the dataset and determine reasonable stopping points. Each iteration found more nondominated designs than the previous, expanding the scope of the concurrent pareto front. Random tests would not have this behavior, as one or two good tests would be likely to dominate all others. The Pareto surfaces for each experiment expanded to cover a wide volume

of data points, something that would not be possible under short timeframes with unoptimized sampling. [Fig. 6 bottom](#) shows the EHVI and hypervolumes for each dataset after each iteration (since EHVI is calculated for every data point, total hypervolumes and expected total hypervolumes can be trivially calculated for the entire dataset). In both cases the initial expected hypervolume improvement from the starting set of alloys was eventually met. The truncated nature of the high SFE experiment suggests that the starting medoids were closer to the ground truth pareto front than in the low SFE case.

Two of the three objectives, strain hardening and hardness, made significant contributions to this hypervolume. One of the findings of this project was that these Al-V-Cr-Fe-Co-Ni materials are largely strain rate insensitive; the SRS average across all materials tested is 7.56×10^{-3} . It is a testament to the Bayesian model's robustness that despite little gain in an objective or values that can mimic the effects of noise, it is still able to successfully optimize other orthogonal properties. Over all five iterations of optimized alloys, their strain hardening ranged from 1.38 to 2.93 GPa, and their hardness ranged from 1.63 to 3.82 GPa. Detailed property tables for all alloys, including overall tension test data, can be found in [Supplementary Information](#).

Several aspects of this work can be expanded upon in future datasets. In order to reduce a large lightly constrained (e.g. 10^5) dataset into one that can be optimized, K-Medoids can be used initially to provide $\sim 1,000$ points that represent the larger feasible space. This results in a phase space broken up into a feasible space and an optimization space; once optimization yields a low resolution Pareto front, areas within the feasible space can be explored to a higher precision now that those families of interesting alloys are found.

BCC and HCP investigations are ripe for research using this method. Furthermore, this method consistently produces a small subset of HEAs that are predicted by CALPHAD to be single phase solid solution when they do not form so experimentally; a growing list of this type of data would be invaluable to CALPHAD engineers. Conversely, this method produces many alloys that are theorized to not exist by popular HEA discovery methods; it is shown in [Supplementary Information](#) how common methods for discovering HEAs fail to predict the successfully fabricated single phase solid solution materials in this work. The existence of previously thought impossible HEAs discovered in this work can be used to expand the utility of those discovery methods.

The framework can begin with 10's or even 100's of millions of alloys. We have internally used ThermoCalc to approach computation rates of 1 million alloys per day even with a small level of parallelization. A dedicated CALPHAD server could steadily model a phase space with a finer resolution, providing millions of points of data. Using the aforementioned K-Medoids method, this complex space can effectively be explored despite being so populous.

Perhaps most importantly, while an HEA was provided as a case study, no aspect of this Bayesian framework hinges on atomic disorder or even the fact that the subject is a metal. Steels, SMAs, ceramics, and polymers could all be explored, making this an effective generalized framework for discovery in Materials Science.

Methods

Fabrication

All designed alloys were synthesized from high-purity elements (>99.9 wt.%) using an Edmund Bühler Arc Melter AM 200 Vacuum Arc Melting system (VAM) into 30 gram ingots. To achieve an acceptable level of mixing of the elements, each ingot was flipped and remelted 7 times. Homogenization heat treatments were performed using a Centorr high temperature furnace (LF Series, Model 22) under an Ar atmosphere with three chamber purges each. The ingots were hot forged at 1150 °C, yielding an approximate 65% thickness reduction. Sample profiles were cut via wire electrical discharge machining (wire-cut EDM) to produce flat tension test coupons (a variation of SS-3 tension specimens^{33, 34}) with gauge dimensions of 8 mm x 3 mm x 1 mm and a cross-sectional slice for electron microscopy (SEM/EDX), X-ray Diffraction (XRD), Vickers Microhardness, and nanoindentation.

Phase & Composition Analysis

Samples were polished for microscopy with a Buehler AutoMet 250 autopolisher and Buehler Vibromet 2 vibratory polisher. Micrographs of each alloy were taken with a Phenom XL scanning electron microscope (SEM) with compositional measurements via an energy-dispersive x-ray spectroscopy detector (EDS). Backscattered electron images were taken of each of the samples at 2,000x magnification of the undeformed alloys. X-ray diffraction (XRD) data was obtained with a Bruker D8 Discover diffractometer at room temperature equipped with a Cu K- α X-ray source and a Vantec 500 area detector. EBSD of the samples was performed using a Tescan FERA-3 Model GMH Focused Ion Beam Microscope. Microscopy images and graphs are included in [Supplementary Information](#).

Mechanical Analysis

Isothermal tension tests were performed with an MTS hydraulic tension test system with a 2500 lbf (11.12 kN) load cell at a strain rate of $5 \times 10^{-4} \text{ s}^{-1}$ and with an MTS extensometer directly attached to the gauge section of the specimens. True σ - ϵ curves for each alloy were plotted to obtain the true stress at engineering ultimate tensile stress (UTS) and the yield stress (YS) at 0.2% offset in order to determine strain hardening (unitless) (included in [Supplementary Information](#)). Each sample was indented with a KLA Instruments iMicro nanoindenter (NI) using a Berkovich diamond tip. Optical photos were taken of nanoindents with a Keyence VK- X1000 3D Surface Profiler. Hardness (in GPa) was computed from the peak load in the nanoindentation test divided by the projected contact area measured optically. Strain rate sensitivities (unitless) were calculated across several orders of magnitude via the NI strain rate jump test (SRJT) method³⁵. The strain rate jump test method (SRJT) for nanoindentation tests was taken in preference to standard nanoindentation methods since it fully accounts for pile-up around the hardness impression, a phenomenon common to HEAs that would otherwise lead to reporting hardness from inaccurate area measurements. Property values are included in [Supplementary Information](#).

Modeling Parameters

Gaussian Processors were instantiated with a Squared Exponential kernel and EHVI acquisition function, with length scales ranging from 0.05 to 0.95 inclusive and standard deviations (the root of the scaling factor for the squared exponential kernel) equal to one half of 1.2x the maximum value for each objective. Standard deviations were updated with each iteration. Strain rate sensitivity values were multiplied by 100 prior to model input to put them on a similar scale to the other objectives.

Data Availability

The data within this study is included in [Supplementary Information](#).

Code Availability

Code for this project is available on GitHub at <https://github.com/trevorhastings/HTMDEC>.

References

1. Rao ZY, Tung PY, Xie RW, Wei Y, Zhang HB, Ferrari A, et al. Machine learning-enabled high-entropy alloy discovery. *Science*. 2022;378(6615):78-84.
2. Yi L, Jiong W, Bin X, Jintao S. Accelerated development of hard high-entropy alloys with data-driven high-throughput experiments. *Journal of Materials Informatics*. 2022;2(1):3.
3. Giles SA, Sengupta D, Broderick SR, Rajan K. Machine-learning-based intelligent framework for discovering refractory high-entropy alloys with improved high-temperature yield strength. *NPJ COMPUTATIONAL MATERIALS*. 2022;8(1).
4. Wen C, Zhang Y, Wang C, Xue D, Bai Y, Antonov S, et al. Machine learning assisted design of high entropy alloys with desired property. *Acta Materialia*. 2019;170:109-17.
5. Yang C, Ren C, Jia Y, Wang G, Li M, Lu W. A machine learning-based alloy design system to facilitate the rational design of high entropy alloys with enhanced hardness. *Acta Materialia*. 2022;222:117431.
6. del Rosario Z, Rupp M, Kim Y, Antono E, Ling J. Assessing the frontier: Active learning, model accuracy, and multi-objective candidate discovery and optimization. *JOURNAL OF CHEMICAL PHYSICS*. 2020;153(2).
7. Gopakumar AM, Balachandran PV, Xue DZ, Gubernatis JE, Lookman T. Multi-objective Optimization for Materials Discovery via Adaptive Design. *SCIENTIFIC REPORTS*. 2018;8.
8. Jablonka KM, Jothiappan GM, Wang SF, Smit B, Yoo B. Bias free multiobjective active learning for materials design and discovery. *Nat Commun*. 2021;12(1).
9. Li HC, Yuan RH, Liang H, Wang WY, Li JS, Wang J. Towards high entropy alloy with enhanced strength and ductility using domain knowledge constrained active learning. *MATERIALS & DESIGN*. 2022;223.
10. Shahriari B, Swersky K, Wang Z, Adams RP, Freitas Nd. Taking the Human Out of the Loop: A Review of Bayesian Optimization. *Proceedings of the IEEE*. 2016;104(1):148-75.
11. Erps T, Foshey M, Luković MK, Shou W, Goetzke HH, Dietsch H, et al. Accelerated discovery of 3D printing materials using data-driven multiobjective optimization. *Science Advances*. 7(42):eabf7435.
12. Sohn SS, Kwiatkowski da Silva A, Ikeda Y, Körmann F, Lu W, Choi WS, et al. Ultrastrong Medium-Entropy Single-Phase Alloys Designed via Severe Lattice Distortion. *Advanced Materials*. 2019;31(8):1807142.
13. Han Z, Ding C, Liu G, Yang J, Du Y, Wei R, et al. Analysis of deformation behavior of VCoNi medium-entropy alloy at temperatures ranging from 77 K to 573 K. *Intermetallics*. 2021;132:107126.
14. Li J, Lu K, Zhao X, Ma X, Li F, Pan H, et al. A superior strength-ductility synergy of Al_{0.1}CrFeCoNi high-entropy alloy with fully recrystallized ultrafine grains and annealing twins. *Journal of Materials Science & Technology*. 2022;131:185-94.
15. Liu T, Chen R, Gao X, Fang H, Qin G, Su Y, et al. Formation of hypoeutectic structure and strengthening mechanism of Co₄Cr_{1.5}Fe_{1.5}Ni₅ high entropy alloy alloyed by Al. *Journal of Alloys and Compounds*. 2022;923:166372.
16. Wang W-R, Wang W-L, Wang S-C, Tsai Y-C, Lai C-H, Yeh J-W. Effects of Al addition on the microstructure and mechanical property of Al_xCoCrFeNi high-entropy alloys. *Intermetallics*. 2012;26:44-51.
17. Zhang Y, Zhou YJ, Lin JP, Chen GL, Liaw PK. Solid-Solution Phase Formation Rules for Multi-component Alloys. *Advanced Engineering Materials*. 2008;10(6):534-8.
18. Redlich O, Kister AT. Algebraic Representation of Thermodynamic Properties and the Classification of Solutions. *Industrial & Engineering Chemistry*. 1948;40(2):345-8.
19. Saleh G, Kvashnin AG, Oganov AR. *Computational materials discovery: Royal Society of Chemistry*; 2018.
20. Tsai M-H, Yeh J-W. High-Entropy Alloys: A Critical Review. *Materials Research Letters*. 2014;2(3):107-23.
21. Senkov ON, Miller JD, Miracle DB, Woodward C. Accelerated exploration of multi-principal element alloys with solid solution phases. *Nat Commun*. 2015;6(1):6529.
22. Gao MC, Zhang B, Yang S, Guo SM. Senary Refractory High-Entropy Alloy HfNbTaTiVZr. *Metallurgical and Materials Transactions A*. 2016;47(7):3333-45.
23. Zhang F, Zhang C, Chen SL, Zhu J, Cao WS, Kattner UR. An understanding of high entropy alloys from phase diagram calculations. *Calphad*. 2014;45:1-10.
24. Zhang C, Zhang F, Chen S, Cao W. Computational Thermodynamics Aided High-Entropy Alloy Design. *JOM*. 2012;64(7):839-45.
25. Zhang B, Gao MC, Zhang Y, Yang S, Guo SM. Senary refractory high entropy alloy MoNbTaTiVW. *Materials Science and Technology*. 2015;31(10):1207-13.
26. Bracq G, Laurent-Brocq M, Perrière L, Pirès R, Joubert J-M, Guillot I. The fcc solid solution stability in the Co-Cr-Fe-Mn-Ni multi-component system. *Acta Materialia*. 2017;128:327-36.
27. Gao MC, Carney CS, Dogan AN, Jablonksi PD, Hawk JA, Alman DE. Design of Refractory High-Entropy Alloys. *JOM*. 2015;67(11):2653-69.
28. Khan TZ, Kirk T, Vazquez G, Singh P, Smirnov AV, Johnson DD, et al. Towards stacking fault energy engineering in FCC high entropy alloys. *Acta Materialia*. 2022;224:117472.
29. Park H-S, Jun C-H. A simple and fast algorithm for K-medoids clustering. *Expert Systems with Applications*. 2009;36(2, Part 2):3336-41.

30. Khatamsaz D, Vela B, Singh P, Johnson DD, Allaire D, Arróyave R. Bayesian optimization with active learning of design constraints using an entropy-based approach. *npj Computational Materials*. 2023;9(1):49.
31. Zhao G, Arroyave R, Qian X. Fast Exact Computation of Expected HyperVolume Improvement. 2018.
32. Patel JK, Read CB. Handbook of the normal distribution. 2nd ed., rev. and expanded. ed: Marcel Dekker; 1996.
33. Gussev MN, Howard RH, Terrani KA, Field KG. Sub-size tensile specimen design for in-reactor irradiation and post-irradiation testing. *Nuclear Engineering and Design*. 2017;320:298-308.
34. Klueh RL. Miniature tensile test specimens for fusion reactor irradiation studies. *Nuclear Engineering and Design Fusion*. 1985;2(3):407-16.
35. Maier V, Durst K, Mueller J, Backes B, Höppel HW, Göken M. Nanoindentation strain-rate jump tests for determining the local strain-rate sensitivity in nanocrystalline Ni and ultrafine-grained Al. *Journal of Materials Research*. 2011;26(11):1421-30.

Acknowledgements

This work was supported by funding provided by the HTMDEC program. We would like to acknowledge Dr. Anup and his group for at Texas A&M University for use of their XRD Bruker D8 Discover instrument as well as Texas A&M's Materials Characterization Facility for use of their EBSD-capable FIB-SEM. We would like to acknowledge Texas A&M's High Performance Research Computing group for access to the parallelization clusters needed for the models in this project.

Author Information

Conceptualization, R.A., I.K., A.S.; Methodology, R.A., I.K., J.P., B.B., G.P., D.A; Modeling, T.H., M.M.; Production, D.S., M.S.; Formal Analysis, T.H., M.M. D.S, W.X., D.L., N.P., B.M., B.B.; Optimization, D.K.; Writing – Original Draft, T.H.; Writing – Review & Editing, T.H., M.M., J.P., B.B.

Ethics Declarations

The authors declare no competing interests

Appendix

Contents

S1 COMPOSITIONS FOR ALL ALLOYS	2
Supplementary Table 1 Iteration 1 alloys	
Supplementary Table 2 Iteration 2 alloys	
Supplementary Table 3 Iteration 3 alloys	
Supplementary Table 4 Iteration 4 alloys	
Supplementary Table 5 Iteration 5 alloys	
Supplementary Figure 1 XRD data for all alloys	
Supplementary Figure 2 Example SEM micrographs	
S2 PROPERTIES FOR ALL ALLOYS.....	6
Supplementary Table 6 Iteration 1 alloy properties	
Supplementary Table 7 Iteration 2 alloy properties	
Supplementary Table 8 Iteration 3 alloy properties	
Supplementary Table 9 Iteration 4 alloy properties	
Supplementary Table 10 Iteration 5 alloy properties	
Supplementary Figure 3 Tensile tests for all alloys	
S3 PARETO SURFACES	8
Supplementary Equation 1 The Pareto front	
Supplementary Figure 4 3D Pareto surfaces	
S4 SIZE OF THE HEA SPACE.....	10
Supplementary Table 11 Number of unique ways of partitioning d identical parts into n bins.	
Supplementary Equation 2 Partition function for 6 bins	
Supplementary Equation 3 Generalized partition function	
Supplementary Equation 4 Example polynomials with Stirling coefficients	
Supplementary Figure 5 Common sizes of compositional lists	
S5 VISUALIZATION OF HIGHER DIMENSIONAL SPACES.....	12
Supplementary Figure 6 UMAP constructions.	
S6 OTHER METHODS OF PREDICTING SINGLE PHASE SOLID SOLUTION HEAS	13
Supplementary Equation 5 Modified Hume-Rothery rules	
Supplementary Figure 7 Al–V–Cr–Fe–Co // Ni pseudo-binary phase diagram	
Supplementary Figure 8 Al–V, Al–Cr, Al–Fe binary phase diagrams	
Supplementary Equation 6 Enthalpy of formation	
Supplementary Figure 9 Minimum binary compound ΔH_f in meV/atom relative to pure elements	
S7 THERMODYNAMIC DATABASES SUITABLE FOR HEAS	16
Supplementary Table 12 List of commercially available CALPHAD ternary assessments	
S8 SFE MODEL.....	16
REFERENCES.....	17

S1 COMPOSITIONS FOR ALL ALLOYS

Composition and structure information for all alloys tested in this work are listed in [Supplementary Tables 1-5](#).

Supplementary Table 1 | Iteration 1 alloys

Alloy Name	Target Atomic %						EDS Measured Atomic %						Phase	Deformation
	Al	V	Cr	Fe	Co	Ni	Al	V	Cr	Fe	Co	Ni		
AAA01	0	10	10	20	45	15	0	10.3	10.4	20.3	44.4	14.5	FCC	Ductile
AAA02	0	10	10	5	30	45	0	10.4	10.4	5.2	30.2	43.9	FCC	Ductile
AAA03	0	15	5	30	30	20	0	15.3	5.3	30.1	29.8	19.5	FCC	Ductile
AAA04	0	5	10	20	25	40	0	5.2	10.4	20.2	25.2	39.0	FCC	Ductile
AAA05	0	0	10	55	10	25	0	0	10.6	54.8	10.1	24.5	FCC	Ductile
AAA06	0	5	25	5	35	30	0	5.2	25.6	5.0	34.9	29.3	FCC	Ductile
AAA07	0	10	10	10	55	15	0	10.3	10.3	10.1	54.7	14.6	FCC	Ductile
AAA08	0	5	10	25	10	50	0	5.3	10.5	25.5	10.2	48.4	FCC	Ductile
AAA09	5	5	5	25	0	60	5.5	5.3	5.2	25.5	0	58.6	FCC	Ductile
AAA10	0	5	15	5	5	70	0	5.1	15.5	5.2	5.2	69.0	FCC	Ductile
AAA11	0	5	5	45	15	30	0	5.2	5.2	45.1	15.2	29.3	FCC	Ductile
AAA12	5	5	5	5	15	65	5.3	5.1	5.3	5.2	15.2	63.8	FCC	Ductile
AAA13	5	5	5	25	10	50							FCC	Brittle
AAA14	0	25	10	5	25	35	0	25.2	10.1	5.0	24.9	34.8	FCC	Ductile
AAA15	5	0	5	45	0	45	4.9	0	5.4	45.5	0	44.2	FCC	Ductile
AAA16	0	20	10	10	5	55	0	20.0	10.1	10.1	5.0	54.7	FCC	Ductile

Supplementary Table 2 | Iteration 2 alloys

Alloy Name	Target Atomic %						EDS Measured Atomic %						Phase	Deformation
	Al	V	Cr	Fe	Co	Ni	Al	V	Cr	Fe	Co	Ni		
AAB01	0	10	10	15	50	15	0	10.2	10.2	15.3	49.6	14.7	FCC	Ductile
AAB02	0	0	0	75	5	20							BCC	Ductile
AAB03	0	5	10	35	25	25	0	5.1	10.2	35.2	24.8	24.7	FCC	Ductile
AAB04	0	5	10	25	25	35	0	5.1	10.2	25.2	24.9	34.5	FCC	Ductile
AAB05	0	10	5	10	25	50	0	10.1	5.1	10.1	25.1	49.6	FCC	Ductile
AAB06	0	5	20	5	30	40	0	5.1	20.5	5.1	29.9	39.3	FCC	Ductile
AAB07	0	10	15	5	40	30	0	10.1	15.3	5.1	40.0	29.5	FCC	Ductile
AAB08	0	5	10	30	5	50	0	5.1	10.3	30.2	5.1	49.4	FCC	Ductile
AAB09	0	5	0	30	30	35	0	5.1	0	30.5	29.9	34.4	FCC	Ductile
AAB10	5	0	5	25	20	45	5.1	0	5.1	25.3	20.1	44.3	FCC	Ductile
AAB11	0	10	20	10	5	55	0	10.2	20.3	10.2	5.0	54.3	FCC	Ductile
AAB12	0	20	5	20	15	40	0	20.4	5.1	20.2	15.0	39.4	FCC	Ductile
AAB13	5	0	10	35	5	45	5.2	0	10.2	35.2	5.1	44.2	FCC	Ductile
AAB14	5	5	0	30	10	50	5.3	5.1	0	30.3	10.2	49.0	FCC	Ductile
AAB15	5	5	10	20	5	55	4.6	4.9	10.1	20.3	5.1	55.0	FCC	Ductile
AAB16	15	0	0	15	5	65							L ₁₂	Ductile

Supplementary Table 3 | Iteration 3 alloys

Alloy Name	Target Atomic %						EDS Measured Atomic %						Phase	Deformation
	Al	V	Cr	Fe	Co	Ni	Al	V	Cr	Fe	Co	Ni		
AAC01	0	5	25	5	15	50	0	5.1	25.2	5.1	15.1	49.6	FCC	Ductile
AAC02	0	15	5	35	10	35	0	15.0	5.0	35.1	10.0	34.8	FCC	Ductile
AAC03	0	5	20	5	40	30	0	5.1	20.2	5.1	40.1	29.5	FCC	Ductile
AAC04	0	15	15	10	45	15	0	15.1	15.1	10.1	44.8	14.8	FCC	Ductile
AAC05	0	10	0	15	75	0	0	10.2	0	15.4	74.4	0	FCC	Ductile
AAC06	0	10	20	10	25	35	0	10.2	20.3	10.1	24.9	34.4	FCC	Ductile
AAC07	0	10	5	15	45	25	0	9.9	5.1	15.2	45.0	24.7	FCC	Ductile
AAC08	0	15	10	15	30	30	0	15.2	10.1	15.2	29.8	29.6	FCC	Ductile
AAC09	5	5	5	20	10	55	5.2	5.1	5.1	20.3	10.0	54.2	FCC	Ductile
AAC10	0	5	20	5	10	60	0	5.1	20.4	5.1	10.3	59.2	FCC	Ductile
AAC11	0	30	5	5	10	50	0	30.5	5.0	5.0	10.0	49.5	FCC	Ductile
AAC12	0	25	15	5	35	20							DO ₂₂	Brittle
AAC13	0	15	20	5	15	45	0	15.3	20.2	5.1	15.1	44.4	FCC	Ductile
AAC14	0	25	5	15	15	40	0	25.4	5.0	15.1	15.0	39.5	FCC	Ductile
AAC15	5	15	5	20	5	50	5.5	15.1	5.0	20.2	4.9	49.4	FCC	Ductile
AAC16	0	20	15	5	25	35	0	20.4	15.2	5.2	24.9	34.3	FCC	Ductile

Supplementary Table 4 | Iteration 4 alloys

Alloy Name	Target Atomic %						EDS Measured Atomic %						Phase	Deformation
	Al	V	Cr	Fe	Co	Ni	Al	V	Cr	Fe	Co	Ni		
AAO01	0	20	10	10	30	30	0	21.2	10.6	9.9	29.6	28.6	FCC	Ductile
AAO02	0	25	5	15	40	15	0	26.1	5.3	14.9	39.4	14.3	FCC	Ductile
AAO03	0	15	5	30	5	45	0	15.8	5.3	30.4	5.3	43.2	FCC	Ductile
AAO04	0	15	5	25	20	35	0	15.8	5.3	25.2	20.2	33.5	FCC	Ductile
AAO05	0	5	25	10	40	20	0	5.3	26.2	10.0	39.2	19.2	FCC	Ductile
AAO06	0	15	15	10	35	25	0	15.8	15.7	10.0	34.5	24.0	FCC	Ductile
AAO07	0	15	10	10	20	45	0	15.9	10.6	10.1	20.1	43.2	FCC	Ductile
AAO08	0	10	25	15	25	25	0	10.6	26.2	14.7	24.7	23.9	FCC	Ductile
AAO09	0	20	15	5	15	45	0	21.0	15.8	4.9	15.0	43.3	FCC	Ductile
AAO10	0	5	5	30	5	55	0	5.3	5.4	30.9	5.4	53.1	FCC	Ductile
AAO11	0	25	10	5	20	40	0	26.3	10.5	4.9	19.8	38.5	FCC	Ductile
AAO12	0	30	15	0	20	35							FCC + FCC	Brittle
AAO13	5	25	0	5	10	55	3.1	26.6	0	5.2	10.4	54.7	FCC	Ductile
AAO14	0	15	15	15	15	40	0	15.8	15.8	14.9	15.1	38.4	FCC	Ductile
AAO15	0	25	5	10	25	35	0	26.1	5.3	10.0	24.9	33.7	FCC	Ductile
AAO16	0	20	20	10	35	15							FCC + FCC	Brittle

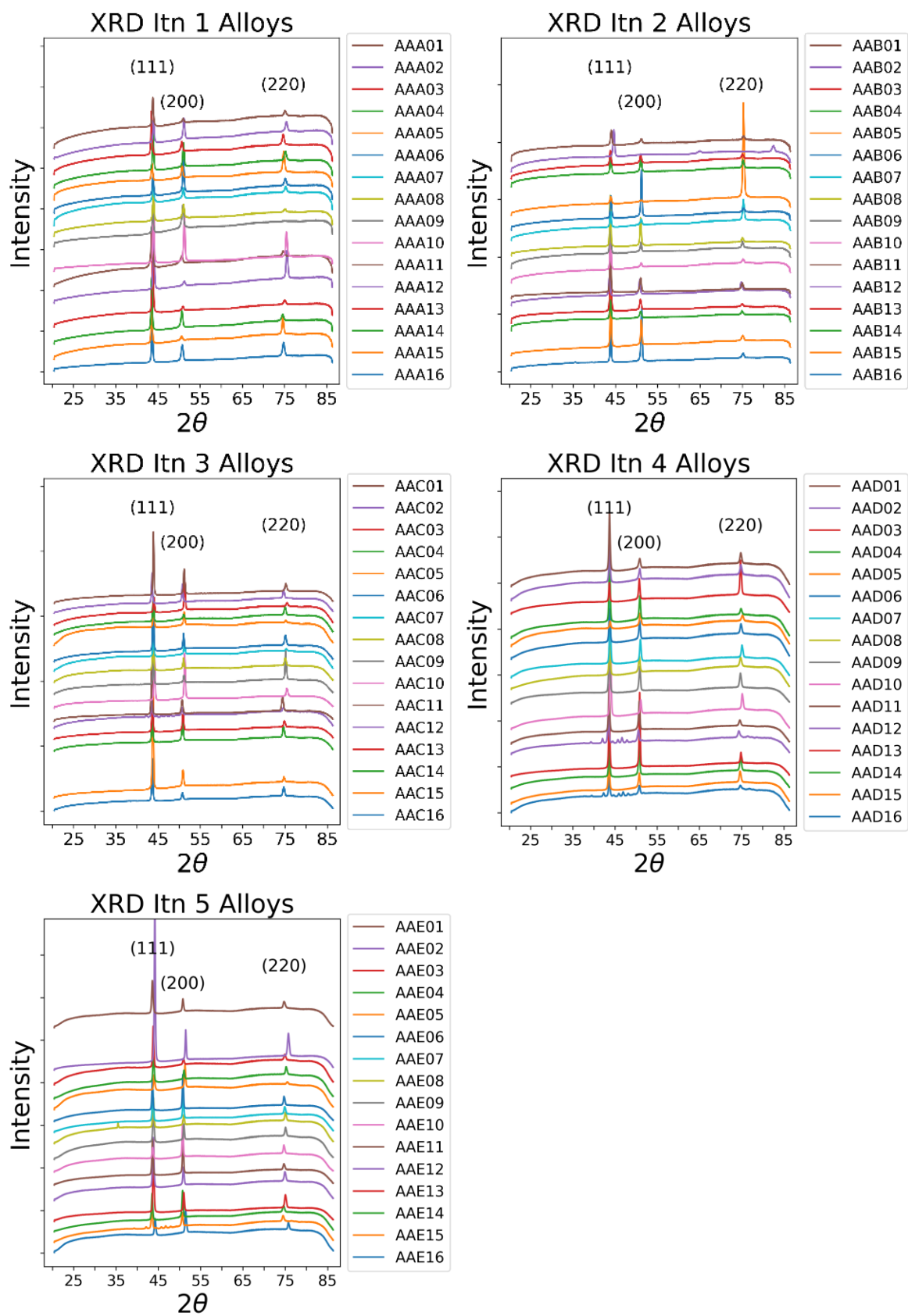
Supplementary Table 5 | Iteration 5 alloys

Alloy Name	Target Atomic %						EDS Measured Atomic %						Phase	Deformation
	Al	V	Cr	Fe	Co	Ni	Al	V	Cr	Fe	Co	Ni		
AAE01	0	0	20	55	0	25	0	0	21.5	55.3	0	23.2	FCC	Ductile
AAE02	0	15	0	0	10	75	0	15.4	0	0	10.6	73.9	BCC	Ductile
AAE03	0	25	5	15	50	5	0	26.0	5.3	15.0	48.8	4.9	FCC	Ductile
AAE04	0	0	20	30	35	15	0	0	20.6	29.9	35.0	14.5	FCC	Ductile
AAE05	0	10	15	0	65	10	0	10.5	15.8	0.0	64.0	9.8	FCC	Ductile
AAE06	0	20	0	30	10	40	0	21.0	0	30.6	10.4	38.0	FCC	Ductile
AAE07	0	10	20	15	15	40	0	10.7	21.2	14.9	15.1	38.1	FCC	Ductile
AAE08	0	20	5	15	40	20							L ₁₂	Ductile
AAE09	0	5	0	35	25	35	0	5.2	0	36.0	25.6	33.3	FCC	Ductile
AAE10	0	20	5	15	20	40	0	20.9	5.3	15.1	20.2	38.4	FCC	Ductile
AAE11	0	25	10	0	20	45	0	26.2	10.4	0.0	20.0	43.5	FCC	Ductile
AAE12	5	5	0	40	5	45	3.9	5.5	0	42.2	5.6	42.8	FCC	Ductile
AAE13	0	20	5	10	10	55	0	20.9	5.4	10.1	10.3	53.3	FCC	Ductile
AAE14	0	15	20	15	20	30	0	15.9	21.1	14.8	19.8	28.5	FCC	Ductile
AAE15	0	30	5	15	30	20							FCC + FCC	Brittle
AAE16	0	5	0	15	30	50	0	5.2	0	15.6	30.9	48.4	FCC	Ductile

Samples (truncating the first two letters) A13, B02, B16, C12, D12, D16, E08, & E15 were not included in Bayesian optimization methods (even if they exhibited superior mechanical properties), as they failed to meet design objectives: either the alloys were not single phase solid solution FCC, or they lacked ductility and a strain hardening value could not be reported, or both.

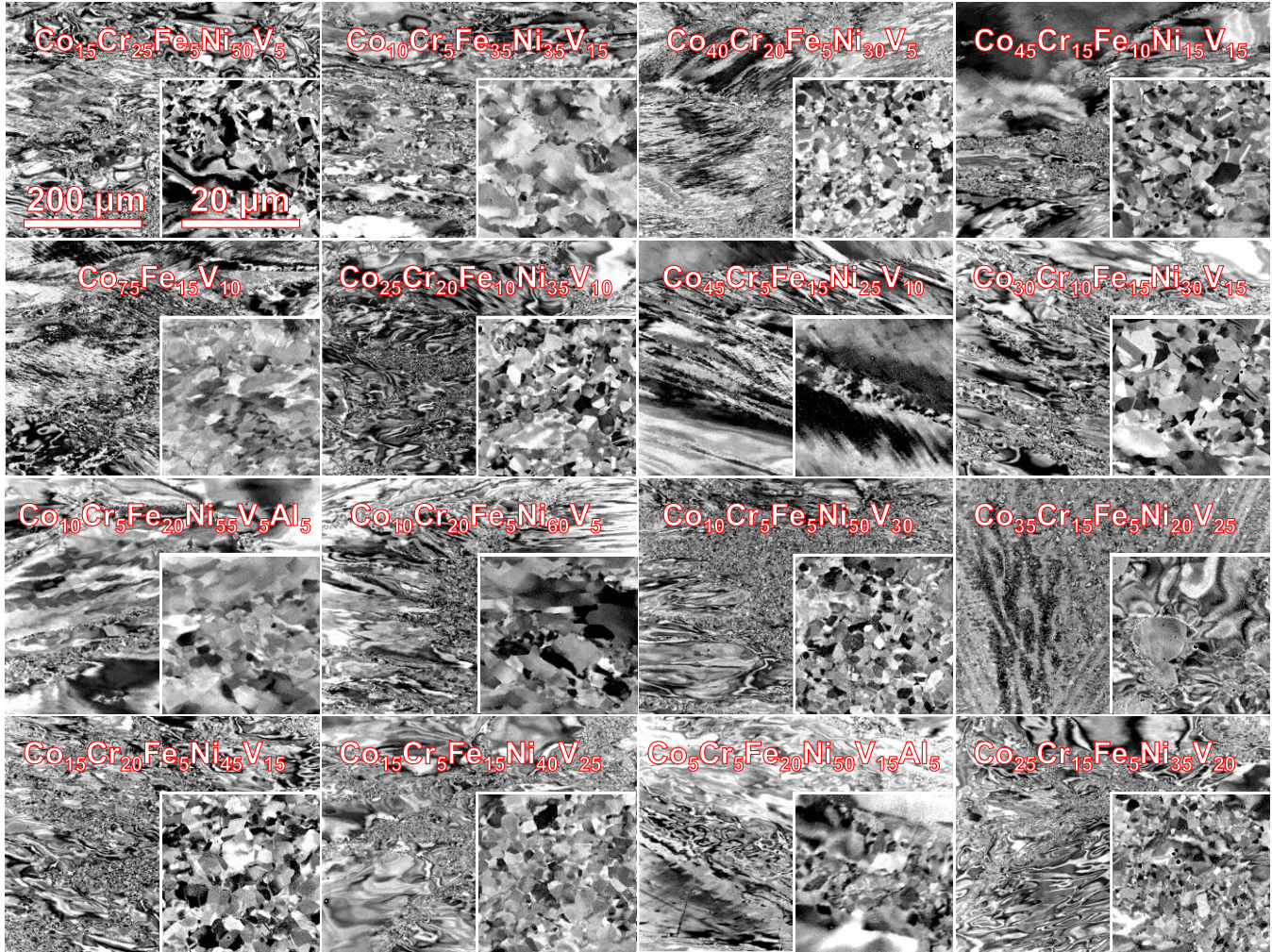
Each of the alloy's XRD peaks are shown in [Supplementary Figure 1](#), verifying the phases listed in [Supplementary Tables 1 - 5](#). Alloy B02's BCC peaks can be seen on either side of the (220) peak. For alloys B16 and E08, their L₁₂ peak can barely be seen ahead of the (111) peak. Dual-FCC multi-peaks can be seen near the (111) peak for all 3 cases.

Supplementary Figure 1 | XRD plots for all alloys



Supplementary Figure 2 | Example SEM micrographs

Back scattered electron micrographs for the 16 alloys of iteration 3. For each case, an inset at the bottom right of the image presents a section with a magnification 10 times larger than the base micrograph. Typically, the inset presents a region recrystallized during the high-temperature thermomechanical processing of the ingots. All samples are single phase with the exception of the alloy C12 (Do₂₂ phase) with a nominal composition of V₂₅Cr₁₅Fe₅Co₃₅Ni₂₀ at.% (3rd row, 4th column), which demonstrates white second phase particles.



S2 PROPERTIES FOR ALL ALLOYS

Property information for all alloys tested in this work are listed in [Supplementary Tables 6-10](#).

Supplementary Table 6 | Iteration 1 alloy properties

Alloy Name	Tension Test Properties				Material Objectives			Pareto	Phase	Deformation
	E (GPa)	YS (MPa)	UTS (MPa)	EL (%)	U / Y	H (GPa)	SRS (x10 ⁻³)			
AAA01	229	487	839	25.7	1.67	2.62	8.17	No	FCC	Ductile
AAA02	220	537	829	20.8	1.66	2.85	7.13	No	FCC	Ductile
AAA03	206	427	721	22.1	1.59	2.40	8.83	No	FCC	Ductile
AAA04	195	383	621	19.5	1.61	2.31	7.01	No	FCC	Ductile
AAA05	162	310	446	18.3	1.38	1.82	8.05	No	FCC	Ductile
AAA06	230	650	974	20.5	1.66	2.90	8.24	No	FCC	Ductile
AAA07	191	606	952	24.9	1.68	2.88	8.57	No	FCC	Ductile
AAA08	189	447	660	14.2	1.57	2.15	7.17	No	FCC	Ductile
AAA09	185	331	782	40.1	2.13	2.31	8.56	Yes	FCC	Ductile
AAA10	205	376	764	28.1	1.90	2.24	6.32	No	FCC	Ductile
AAA11	165	364	547	11.9	1.45	1.91	7.97	No	FCC	Ductile
AAA12	244	391	622	16.7	1.59	2.47	7.46	No	FCC	Ductile
AAA13	185	275	816	0	N/A	2.32	7.90	N/A	FCC	Brittle
AAA14	192	601	1144	29.9	1.91	3.40	8.24	Yes	FCC	Ductile
AAA15	148	253	492	23.3	1.93	1.96	7.73	No	FCC	Ductile
AAA16	199	517	977	26.7	1.78	2.88	8.44	Yes	FCC	Ductile

Supplementary Table 7 | Iteration 2 alloy properties

Alloy Name	Tension Test Properties				Material Objectives			Pareto	Phase	Deformation
	E (GPa)	YS (MPa)	UTS (MPa)	EL (%)	U / Y	H (GPa)	SRS (x10 ⁻³)			
AAB01	230	539	1038	34.6	1.94	2.68	8.36	No	FCC	Ductile
AAB02	185	610	798	3.6	1.31	2.53	12.05	N/A	BCC	Ductile
AAB03	175	363	576	17.2	1.59	2.13	7.02	No	FCC	Ductile
AAB04	193	413	676	20.1	1.64	2.29	6.78	No	FCC	Ductile
AAB05	214	332	634	28.7	1.97	2.35	6.98	No	FCC	Ductile
AAB06	241	508	857	24.4	1.69	2.60	7.52	No	FCC	Ductile
AAB07	221	448	863	28.2	1.93	2.78	7.78	No	FCC	Ductile
AAB08	172	324	604	23.4	1.87	2.11	6.42	No	FCC	Ductile
AAB09	159	347	610	20.0	1.76	1.98	6.97	No	FCC	Ductile
AAB10	167	313	615	24.6	1.98	2.11	6.48	No	FCC	Ductile
AAB11	220	427	886	31.5	2.09	2.62	7.21	No	FCC	Ductile
AAB12	189	430	986	37	2.29	2.71	8.35	Yes	FCC	Ductile
AAB13	179	250	549	27.5	2.19	1.87	7.43	No	FCC	Ductile
AAB14	191	282	691	41.8	2.45	2.25	7.35	Yes	FCC	Ductile
AAB15	221	367	759	33.8	2.10	2.57	7.30	No	FCC	Ductile
AAB16	160	299	333	1.4	1.12	2.97	5.86	N/A	L1 ₂	Ductile

Supplementary Table 8 | Iteration 3 alloy properties

Alloy Name	Tension Test Properties				Material Objectives			Pareto	Phase	Deformation
	E (GPa)	YS (MPa)	UTS (MPa)	EL (%)	U / Y	H (GPa)	SRS (x10 ⁻³)			
AAC01	201	503	854	22.5	1.70	2.82	7.07	No	FCC	Ductile
AAC02	191	391	832	29.7	2.13	2.52	7.86	No	FCC	Ductile
AAC03	216	461	863	26.2	1.89	3.05	7.68	Yes	FCC	Ductile
AAC04	225	569	1044	29.1	1.84	3.17	8.93	Yes	FCC	Ductile
AAC05	199	382	646	27.2	1.70	2.25	8.16	No	FCC	Ductile
AAC06	193	460	932	32.6	2.03	2.73	7.90	No	FCC	Ductile
AAC07	223	357	671	26.6	1.88	2.58	7.42	No	FCC	Ductile
AAC08	213	444	966	33.8	2.18	2.83	8.19	Yes	FCC	Ductile
AAC09	222	366	804	38.4	2.20	2.67	7.77	No	FCC	Ductile
AAC10	240	397	734	22.4	1.85	2.58	6.78	No	FCC	Ductile
AAC11	191	637	1115	25.0	1.75	3.32	7.76	No	FCC	Ductile
AAC12	219	790	790	0	N/A	6.04	6.22	N/A	DO ₂₂	Brittle
AAC13	205	551	1060	31.0	1.93	2.96	7.84	No	FCC	Ductile
AAC14	207	541	1136	33.7	2.10	3.32	7.97	Yes	FCC	Ductile
AAC15	232	542	1006	29.1	1.86	3.35	5.90	No	FCC	Ductile
AAC16	217	613	1197	31.8	1.95	3.29	7.76	No	FCC	Ductile

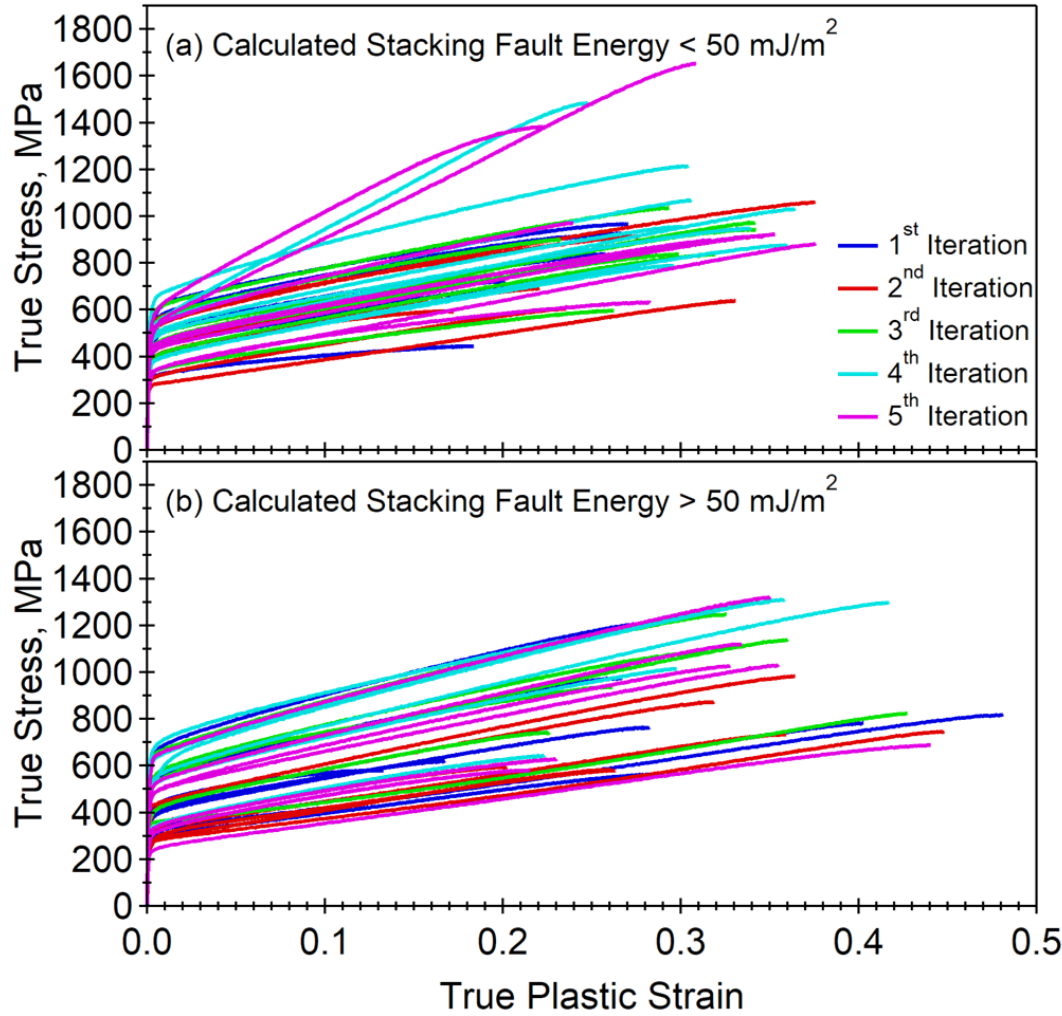
Supplementary Table 9 | Iteration 4 alloy properties

Alloy Name	Tension Test Properties				Material Objectives			Pareto	Phase	Deformation
	E (GPa)	YS (MPa)	UTS (MPa)	EL (%)	U / Y	H (GPa)	SRS (x10 ⁻³)			
AAD01	226	625	1221	31	1.95	3.37	7.23	Yes	FCC	Ductile
AAD02	236	551	1504	24	2.73	3.82	5.62	Yes	FCC	Ductile
AAD03	189	361	842	34	2.33	2.38	7.44	Yes	FCC	Ductile
AAD04	187	391	822	30	2.10	2.30	8.03	No	FCC	Ductile
AAD05	211	502	996	32	1.98	2.77	8.73	Yes	FCC	Ductile
AAD06	191	521	1042	30	2.01	2.94	7.90	Yes	FCC	Ductile
AAD07	210	443	986	34	2.23	2.93	7.28	Yes	FCC	Ductile
AAD08	197	491	945	29	1.93	2.77	8.82	Yes	FCC	Ductile
AAD09	194	525	1142	35	2.17	2.95	8.41	Yes	FCC	Ductile
AAD10	176	308	620	23	2.02	2.15	6.72	No	FCC	Ductile
AAD11	206	590	1274	32	2.21	3.41	7.41	Yes	FCC	Ductile
AAD12	209	559	561	0	N/A	5.96	6.53	N/A	FCC + FCC	Brittle
AAD13	229	669	1164	26	1.74	3.48	6.63	Yes	FCC	Ductile
AAD14	187	459	931	30	2.03	2.57	7.52	No	FCC	Ductile
AAD15	216	614	1311	37	2.13	3.02	8.13	Yes	FCC	Ductile
AAD16	207	460	462	0	N/A	5.22	7.36	N/A	FCC + FCC	Brittle

Supplementary Table 10 | Iteration 5 alloy properties

Alloy Name	Tension Test Properties				Material Objectives			Pareto	Phase	Deformation
	E (GPa)	YS (MPa)	UTS (MPa)	EL (%)	U / Y	H (GPa)	SRS (x10 ⁻³)			
AAE01		318	569	23	1.79	1.63	6.73	No	FCC	Ductile
AAE02		398	899	36	2.26	2.42	6.19	Yes	BCC	Ductile
AAE03		539	1581	27	2.93	3.37	5.55	Yes	FCC	Ductile
AAE04		448	892	31	1.99	2.19	7.97	No	FCC	Ductile
AAE05		548	960	22	1.75	3.09	8.67	No	FCC	Ductile
AAE06		336	850	36	2.53	2.33	8.61	Yes	FCC	Ductile
AAE07		431	895	32	2.08	2.43	7.70	No	FCC	Ductile
AAE08		518	1325	21	2.56	3.42	6.17	N/A	L1 ₂	Ductile
AAE09		305	557	20	1.83	1.80	7.59	No	FCC	Ductile
AAE10		244	644	39	2.64	1.85	7.82	Yes	FCC	Ductile
AAE11		615	1256	36	2.04	3.00	7.92	No	FCC	Ductile
AAE12		477	1062	34	2.23	2.69	8.39	Yes	FCC	Ductile
AAE13		469	1040	33	2.22	2.76	7.35	Yes	FCC	Ductile
AAE14		470	967	31	2.06	2.51	8.72	Yes	FCC	Ductile
AAE15					N/A	4.28	5.95	N/A	FCC + FCC	Brittle
AAE16		339	620	22	1.83	1.92	6.83	No	FCC	Ductile

Supplementary Figure 3 | Tensile tests for all alloys



True stress versus true plastic strain during a room temperature isothermal quasi-static tensile loading till fracture for a selected case for each characterized material. Alloys are grouped in (a) low stacking fault energy ($< 50 \text{ mJ/m}^2$) and (b) high stacking fault energy ($> 50 \text{ mJ/m}^2$) and by Bayesian iteration (1st, blue, 2nd, red, 3rd, green, 4th, cyan, and 5th iteration, magenta). Engineering stress and strain values are listed in Tables S1 through S10.

S3 PARETO SURFACES

Multi-objective design spaces can be understood by the tabulation of each data point that forms a surface of maximal values around the data points that are worse in every aspect. Algebraically, this is known as *dominance*; for an n-dimensional datapoint $p_i = \{x_1, x_2, x_3 \dots\}$ within a set of points S, p_i is considered *nondominated* if there are no other points $q_i \in S$ that have each component x_i greater than its corresponding component in point p. This is formally expressed in [Supplementary Equation 1](#): it reads “For all q in S, if q is not equal to p and it is *not* true that q dominates p with respect to all objective functions, then p belongs in the Pareto front P”. In this case, “dominates” refers to a maximum.

Supplemental Equation 1 | The Pareto front

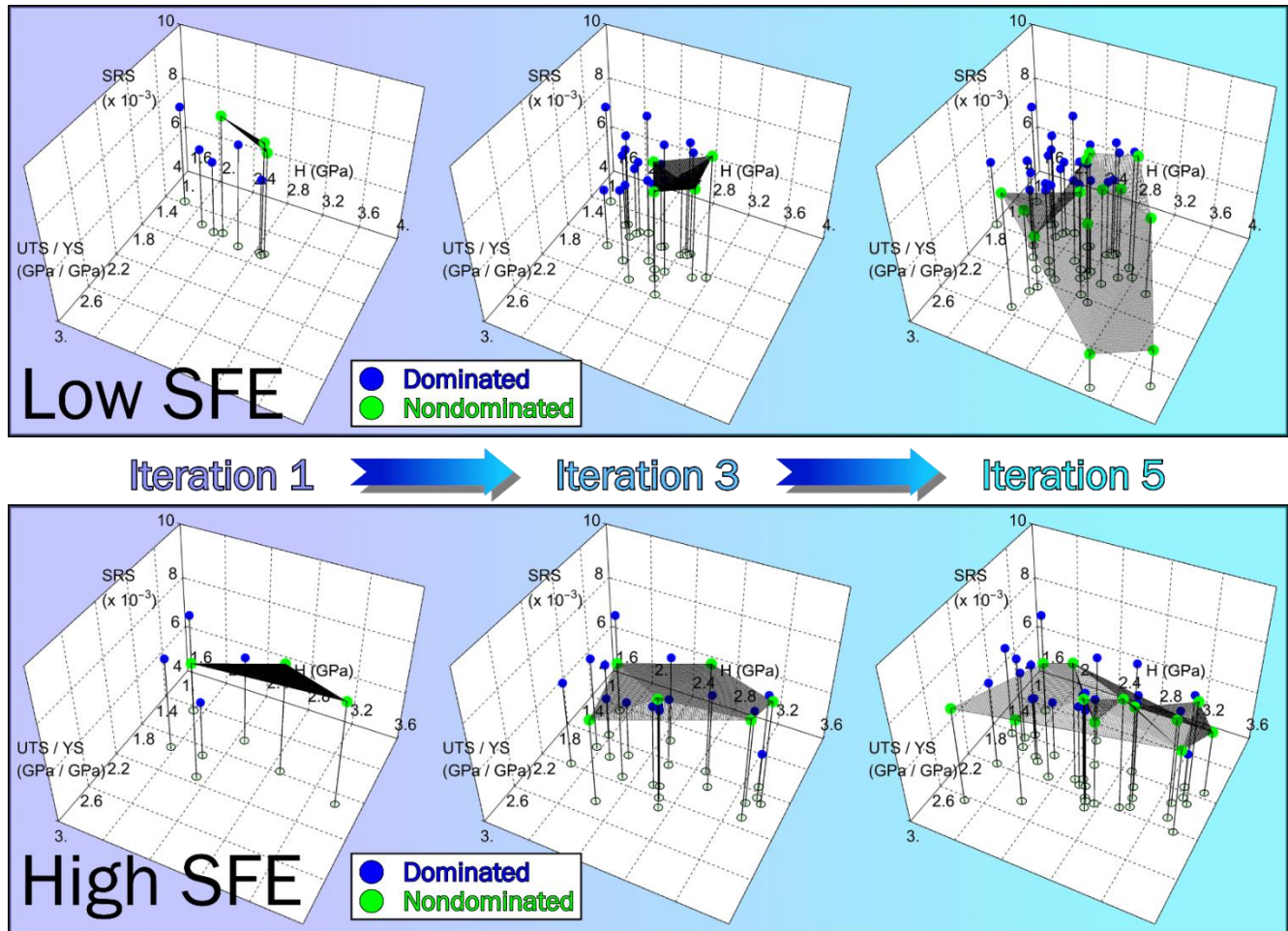
$$\text{Pareto Front } P \equiv \{\forall q_i \in S, q \neq p \wedge \neg(f_1(q) > f_1(p) \wedge f_2(q) > f_2(p) \wedge \dots \wedge f_n(q) > f_n(p)) \rightarrow p_i \in P$$

While typical material applications rarely maximize one property at the extreme cost of all others, such “edge” datapoints are still considered part of the Pareto front; it is not the goal of a HEA Pareto front search to determine

pertinence of each alloy design, but rather to come up with a list of points that have mutually exclusive properties from which to later choose from for further research or industrial purposes.

Supplemental Figure 4 plots the nondominated and dominated points after iterations 1, 3, and 5, with an overlaid pareto surface. Note that this surface is only a visual approximation of the discretized points.

Supplemental Figure 4 | 3D Pareto surfaces



A direct indicator of the optimization technique's success is a suite of new Pareto points with every batch, which Supplemental Figure 4 demonstrates. Despite multiple datapoints not meeting the base criteria in the high SFE experiment, new Pareto points were still found with each iteration. The SRS objective did not optimize as neatly as the others; it is possible that these FCC HEA's are simply not prone to a high level of sensitivity to strain rate. Despite the SRS objective mostly acting as noise within the data, the Bayesian optimization algorithm was able to significantly push a Pareto front in just a few iterations, a testament to the algorithm's stout capacity. A notable misconception regarding the analysis of optimizations is the notion that every objective improve in every iteration. This expressly not the goal, as the BBO method is non-preferential.

In the event that there are concerns about the final Pareto front specifics, such as the idea that some alloys might be too costly to produce, then that is something that should be readdressed with a new optimization problem with an extra dimension.

S4 SIZE OF THE HEA SPACE

Compositional sensitivity has long been exemplified by carbon fractions of small atomic percents being responsible for entire classes of materials. In recent years, phase engineering studies—those involving fine tuning of a composition to achieve an array of properties—have illustrated the importance of finer delineations of atomic fractions. Examples include using DSC to measure near-zero thermal hysteresis or stress-dependent XRD to achieve crystallographic compatibility in 4-element shape memory alloys (10^3 parts).^{1, 2} It is reasonable to assume that these investigations will begin to explore finer regions of their respective compositional spaces, so an exhaustive definition of possible alloys would necessitate dividing each elemental fraction into 10^5 parts. The elements with at least one stable isotope are all found within $Z \leq 83$, the exceptions being technetium, promethium, and bismuth. Removing Tc and Pm, as their most stable isotopes have $t^{1/2} < 10^9$ yr, but keeping Bi, as its most stable half-life is greater than the age of the universe (and is commonly alloyed with other metals) leaves 81 stable elements. Removing the 10 remaining gaseous elements at $T = 25^\circ\text{C}$: {H, He, N, O, F, Ne, Cl, Ar, Kr, Xe} reduces the list to 71. Depending on environmental conditions, the elements that naturally liquify {Ga, Br, Cs, Hg} reduce the list to 67. Despite having low melting points, elements like gallium are regularly alloyed with other metals, yielding an approximate list of 71 elements possible for the fabrication of any alloy imaginable.

Concordantly, one must generate the list of all combinations of elemental compositions divided into 10^5 parts (fractions of 0.00001, or 0.001%) across 71 possible unique containers to express the entire higher dimensional phase space of HEAs (using any production means necessary to achieve a single phase material in each case). This is a resolvable mathematical problem not unique to materials science.

One way to derive this is as follows. One can trivially see that the partition of any number of n bins $\{\{1,1,0,0,0 \dots\}, \{1,0,1,0,0 \dots\} \dots\}$ into $d = 2$ unordered subsets is a simple binomial function “ n choose 2” or $C_2^n = \frac{n!}{2!(n-2)!}$. For $d = 3$, the unordered subsets can consist of combinations $\{\{1,1,1,0,0 \dots\}, \{1,1,0,1,0 \dots\} \dots\}$ or permutations $\{\{2,1,0,0,0 \dots\}, \{1,2,0,0,0 \dots\} \dots\}$ within size n or “ n permute 2” or $P_2^n = (n)(n-1)$. The total number of partitions T for 3 parts becomes the sum of these terms $T(3, d) = C_3^n + P_2^n$. One might naively think that an arbitrary number of partitions could be expressed as a simple sum of combinatorial and permutative terms; it becomes evident that this strategy will no longer be tenable by $d = 8$. It has a total partition of $T(n, 8) = 3P_2^n + 2P_3^n + C_2^n + C_4^n + C_8^n + 2nC_2^n + nC_3^n + nC_4^n + nC_5^n + nC_7^n + 2n(n-1)C_2^n + n(n-1)C_3^n + C_2^nC_2^n + C_3^nC_2^n + C_4^nC_2^n$. Any attempt to define an arbitrary number of partitions would quickly result in a sum of thousands of terms of increasing multinomial complexity with further sums as coefficients.

As an intermediate step, the number of compositions for a given size can be evaluated by numerically defining them in a table. This has the benefit of being error-free and easily accessible for small numbers, but it cannot determine how large the resultant tables of compositions would be for arbitrarily-sized computations. The first few values of $T(n, d)$ are shown in [Supplementary Table 11](#) ($n = 2$ has been skipped as it is merely the sequence of integers).

Supplementary Table 11 | Number of unique ways of partitioning d identical parts into n bins

T	n = 3	n = 4	n = 5	n = 6	n = 7	n = 8	n = 9	OEIS Entry
d = 2	3	6	10	15	21	28	36	A000217
d = 3	7	16	30	50	77	112	156	A005581
d = 4	12	31	65	120	203	322	486	A005718
d = 5	18	52	121	246	455	784	1278	A027659
d = 6	25	80	205	456	917	1708	2994	A062989
d = 7	33	116	325	786	1709	3424	6426	A063267
d = 8	42	161	490	1281	2996	6427	12861	n/a
OEIS Entry	A055998	A092286	n/a	n/a	n/a	n/a	n/a	

The sequences of integers produced by this table, if available on the Online Encyclopedia of Integer Sequences (at the time of this writing) is listed at the end of its corresponding row or column. The simple binomial expression for $d = 2$ constitutes the Triangular Numbers as listed on the OEIS.

“A000217” as listed on the Online Encyclopedia of Integer Sequences (OEIS). As of the time of this writing, the OEIS has documentations for the first six rows and the first 2 columns of [Table 1](#); they are listed in the final row and column and are catalogued in supplemental material. ³ The columns of [Table 1](#) can be fit to polynomials, which Mathematica evaluates with 100% accuracy; an example using $n = 6$ is shown in [Supplementary Equation 2](#). The coefficients of these polynomials are Stirling numbers of the First Kind, and any power of d above $n - 1$ has a coefficient of zero (so they are omitted; in principle the sum can include infinite terms). This is easier to observe with a set of polynomials which are included in supplemental material. The Stirling numbers are easily calculable with a recursion function, so this makes [Supplementary Equation 1](#) generalizable: [Supplementary Equation 2](#) is the total number of partitions for an arbitrary n and d . Note that the constant (with respect to d) factorial term at the end of the sum can also be represented as (*StirlingS1*[$n, 1$] * $(n - 1)$).

Supplementary Equation 2 | Partition function for 6 bins

$$T(6, d) = \left(\frac{1}{(6-1)!}\right) (d^5 + 15d^4 + 85d^3 + 225d^2 + 274d - 600)$$

Supplementary Equation 3 | Generalized partition function

$$T(n, d) = \left(\frac{1}{(n-1)!}\right) \left(\sum_{i=1}^{n-1} (|StirlingS1[n, i + 1]| * d^i) - (n! - (n-1)!)\right)$$

The number of partitions is now known: $T(71, 10^5) \sim 8.56 * 10^{249}$. Ergo, the number of possible compositionally unique HEAs has an upper bound of 10^{250} . Notably, this number is finite. Setting the number of bins constant turns this expression into a polynomial, of which the first few are shown in [Supplementary Equation 4](#).

Supplementary Equation 4 | Example polynomials with Stirling coefficients

$$\{n = 3\} \equiv T = \left(\frac{1}{(n-1)!}\right) (d^2 + 3d - 4)$$

$$\{n = 4\} \equiv T = \left(\frac{1}{(n-1)!}\right) (d^3 + 6d^2 + 11d - 18)$$

$$\{n = 5\} \equiv T = \left(\frac{1}{(n-1)!}\right) (d^4 + 10d^3 + 35d^2 + 50d - 96)$$

$$\{n = 6\} \equiv T = \left(\frac{1}{(n-1)!}\right) (d^5 + 15d^4 + 85d^3 + 225d^2 + 274d - 600)$$

$$\{n = 7\} \equiv T = \left(\frac{1}{(n-1)!}\right) (d^6 + 21d^5 + 175d^4 + 735d^3 + 1624d^2 + 1764d - 4320)$$

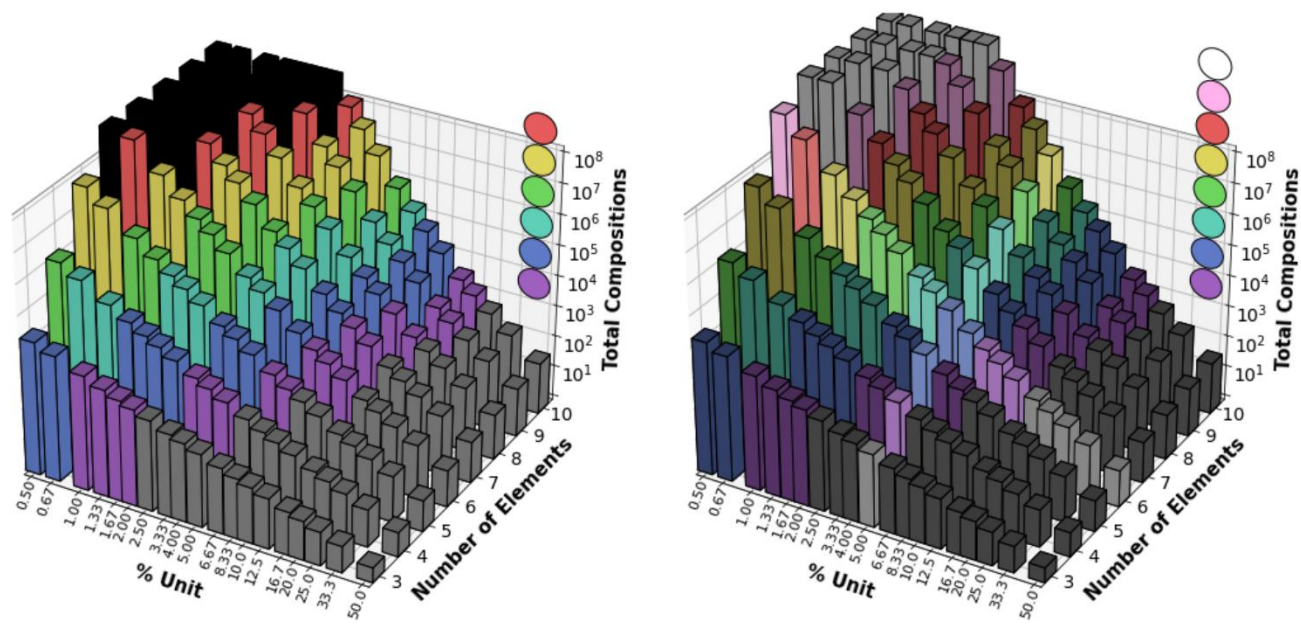
$$\{n = 8\} \equiv T = \left(\frac{1}{(n-1)!}\right) (d^7 + 28d^6 + 322d^5 + 1960d^4 + 6769d^3 + 13132d^2 + 13068d - 35280)$$

$$\{n = 9\} \equiv T = \left(\frac{1}{(n-1)!}\right) (d^8 + 36d^7 + 546d^6 + 4536d^5 + 22449d^4 + 67284d^3 + 118124d^2 + 109584d - 322560)$$

$$\{n = 10\} \equiv T = \left(\frac{1}{(n-1)!}\right) (d^9 + 45d^8 + 870d^7 + 9450d^6 + 63273d^5 + 269325d^4 + 723680d^3 + 1172700d^2 + 1026576d - 3265920)$$

[Supplementary Fig. 5 \(left\)](#) elucidates the computational weight of common partitions of elemental spaces down to 0.5% for a small selection of elements. This simulates a typical design space for HEAs. [Supplementary Fig. 5 \(right\)](#) has a modified color scheme to illuminate the parameters for this project. This visual acts as a useful project design tool: it makes it easy to see at a glance if adding an element or increasing the atomic search resolution will result in a composition list that would be too costly or time consuming to model. It takes few ambitions to suddenly generate a composition list relevant to today’s experimental standards that goes beyond current computational capacities⁴. While this prototype framework showcases an approachable $\sim 10^4$ design space, it can be expanded by several orders of magnitude: 20 core parallelized stress tests using Texas A&M’s High Research Computing Center allowed for the evaluation of alloy systems at rates as high as 800,000 compositions per day for ThermoCalc’s Property Model evaluator. Thus, per [Supplementary Fig. 5](#), regions up to the green color (greater than 1 million, but less than 10 million) would make for approachable design projects.

Supplemental Figure 5 | Common sizes of compositional lists given a number of elements and atomic resolution.

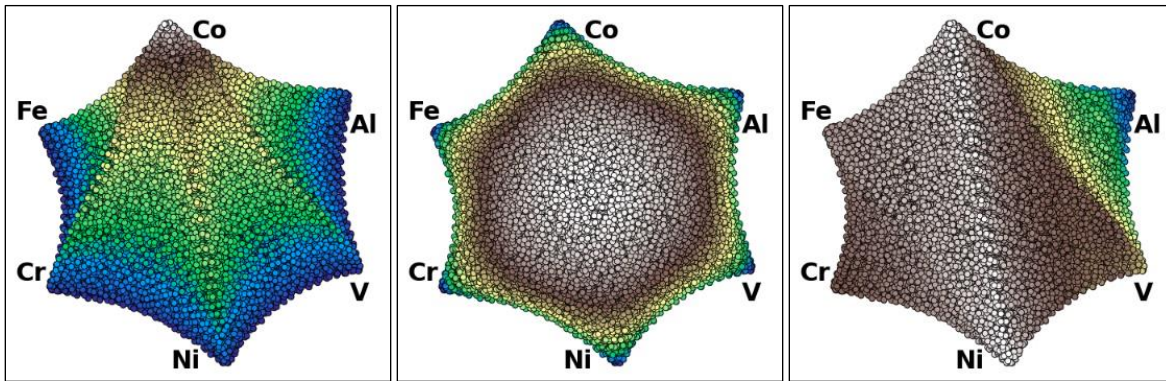


S5 VISUALIZATION OF HIGHER DIMENSIONAL SPACES

One of the core problems of working with n -dimensional spaces is the inability to present all of the data points in their native format when graphed. Some form of information loss is necessitated, often facilitated by dimensionality reduction algorithms (DRAs). The most popular DRA, Principal Component Analysis (PCA) has often been used for its incredible speeds and retainment of information. Unfortunately, PCA-reduced datasets are drawn with arbitrary eigenvectors as axes—an utterly inexplicable coordinate system to the human mind—providing the reader with mostly qualitative assessments of data at a glance. Uniform Manifold Approximation and Projection (UMAP) is a recently developed DRA that attempts to solve these problems while being comparable to PCA in performance.^{5, 6}

UMAP takes its data points and reconstructs them using a topological theory involving each data point's nearest neighbors, wherein it begins with the (naturally false) assumption that the data is uniformly distributed, modifying the space itself between points to relax that assumption. A pertinent feature of this lies in the construction of polygons with concave circular arc edges, where their vertices represent our n -element system's unary epicenters, shown in [Supplementary Figure 5](#). [Supplementary Figure 5a](#) is an example of a UMAP of the 6-dimensional with 53,124 compositions, sorted by Co content. This system, despite having $\sim 10^4$ data points stacked on top of each other, gives the reader an intuitive understanding of fractional compositions: alloys nearly 1.00 mole fraction of an element will lie near that element's vertex while high entropy alloys are moved toward the center. Binary alloys are easily visible along line segments connecting any two elements. Given these qualities, the reader should already be familiar with configurational entropy S_{conf} graph in [Supplementary Figure 5b](#); as expected, higher entropy compositions are in the center. Simple, stoichiometric quantities are similarly visualized. [Supplementary Figure 5c](#) is a colored plot of the alloys' densities; one would expect the binary system containing the highest densities (Co & Ni) to be higher than any of the other data points, and similarly compositions mostly Al to be low, which is correctly intuited by UMAP. In this context UMAP presentations become indisputably less enigmatic than their counterparts.

Supplementary Figure 6 | UMAP constructions



(a) Sorted (and colored) by cobalt fraction. (b) Sorted by entropy (ascending). (c) Sorted by density. (d) Sorted by FCC fraction with only the alloys with cobalt fraction equal to zero displayed.

S6 OTHER METHODS OF PREDICTING SINGLE PHASE SOLID SOLUTION HEAS

There have been many ways to predict HEA phase stability, including: building off of the Hume-Rothery rules^{7, 8, 9, 10, 11, 12}, inspecting binary phase diagram constituents^{13, 14, 15, 16}, and computing first order approximations as an extension of known databases^{17, 18, 19, 20}.

The aforementioned Hume-Rothery variant can be described by interaction between atomic fraction and empirical radii, and regular solution model interaction parameters from literature. [Supplementary Equation 5](#) can be used on the 53,124 compositions for the HEA studied in this work.

Supplementary Equation 5 | Modified Hume-Rothery equations

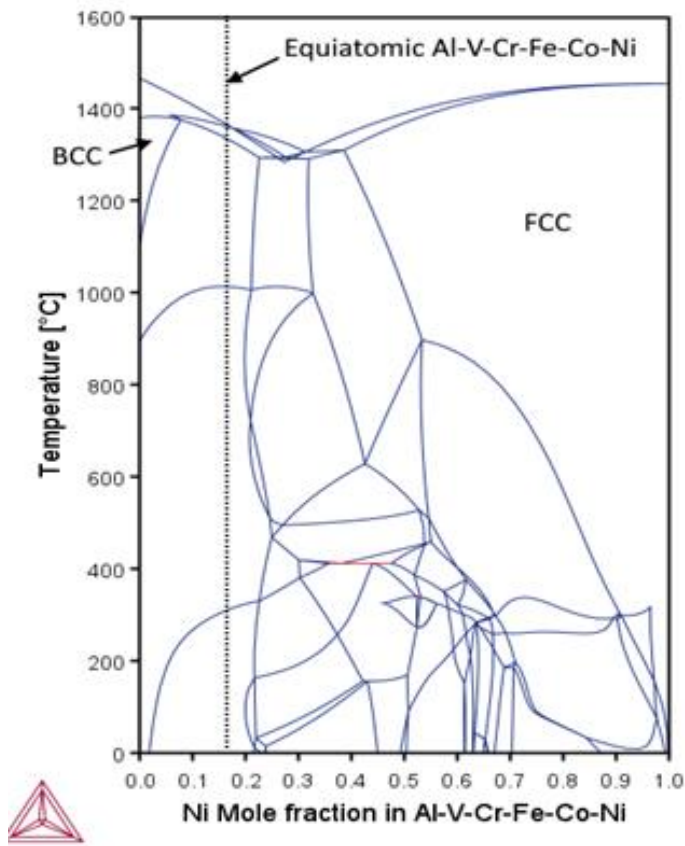
$$\delta = \sqrt{\sum_{i=1}^n c_i \left(1 - \frac{r_i}{\sum_{i=1}^n (c_i r_i)}\right)^2}$$

$$\Omega = \frac{T_m \Delta S_{\text{mix}}}{\Delta H_{\text{mix}}}$$

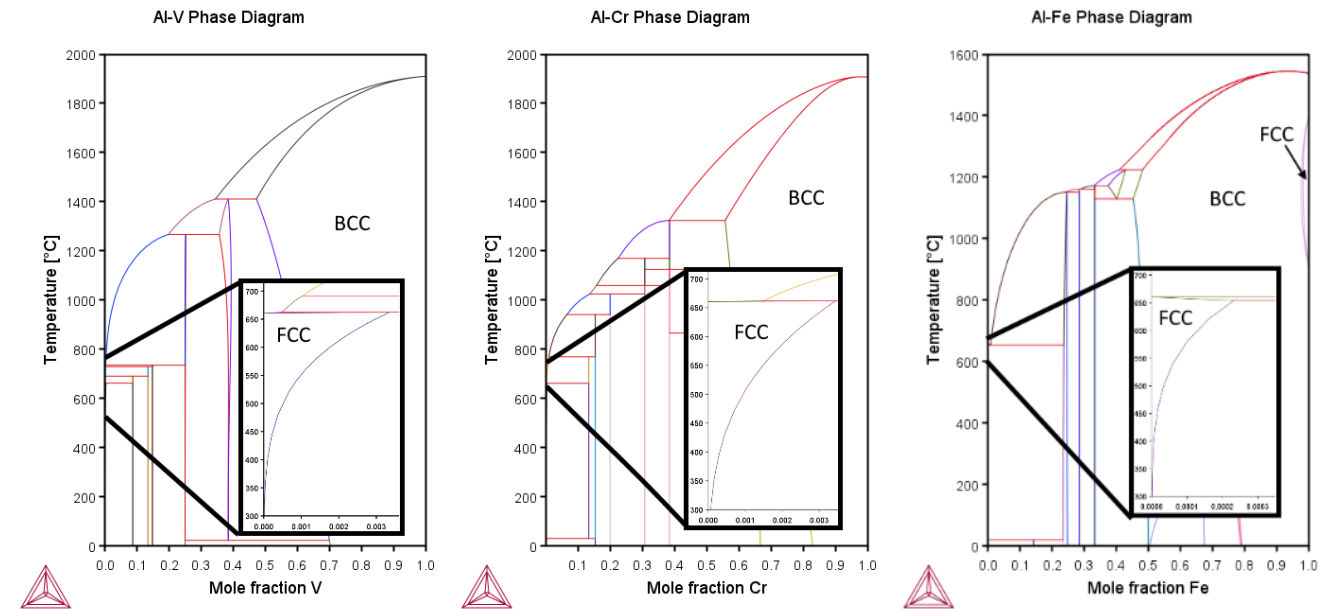
The modified Hume-Rothery parameters have the problem of leniency: this method estimates that ~40,000 of the 53,124 alloys modeled in this work would turn out to be FCC, and that over 15,000 alloys would still be FCC at 700°C, a stark comparison to the <2,500 calculated by ThermoCalc.

The inspection of binary phase diagrams would proceed as follows: if every possible binary alloy within the subsystems of an arbitrary HEA space all exhibit isomorphous solid solutions of a notable phase, a nontrivial solubility of that phase within one element, or a homogeneous range (e.g. >5 at.%) of that phase anywhere within the phase diagram, then one can speculate that this phase is a salient facet of the higher order system. [Supplementary Figure 6](#) shows a pseudo-binary of the system investigated in this work. [Supplementary Figure 7](#) shows 3 of the constituent binaries that violate the above supposition.

Supplementary Figure 7 | Al-V-Cr-Fe-Co // Ni pseudo-binary phase diagram



Supplementary Figure 8 | Al-V, Al-Cr, & Al-Fe binary phase diagrams.



Each of these binaries suggests that FCC should not be possible, as there is an intolerably small amount of V, Cr, or Fe solubility in their terminal FCC phases. While it's unlikely that ThermoCalc's representation of the finer workings of its phase space are accurate, given the large terminal homogeneous FCC region, a single phase with a substantive amount of nickel is expected across a variety of compositions and annealing temperatures, which is what the vast majority of HEAs fabricated verify.

The method involving first order approximations comes from a DFT model of binary enthalpies. As long as the configurational contribution of a system is lower than its lowest DFT evaluated binary subsystem, then it will have a single phase present (and conversely, the reverse of this indicates *no* single phases can be present). For example, an equiatomic Cr–Fe–Co–Ni HEA annealed at 700 °C results in an enthalpy of -116 meV/atom, while the lowest DFT binary enthalpy formation for this system is -97 meV/atom, supporting the conclusion that such an HEA would be single phase. Adding aluminum to this alloy suggests phase separation, as its configuration term is -135 eV/atom while the Al–Ni DFT calculation is -677 meV/atom. This has been experimentally verified for some compounds.²⁰

Supplementary Equation 6, enthalpy of formation, is then used to determine phase stability. As long as the configurational contribution of a system is lower than its lowest evaluated binary subsystem using DFT, then a single homogenous phase will be present. Supplementary Figure 8 shows the formation enthalpies for the binary compounds subsisting within the space tested within this work.

Supplementary Equation 6 | Enthalpy of formation

$$\Delta H_{\text{formation}} \geq -T\Delta S_{\text{mix ideal}} = -RT \sum_{i=1}^n X_i \ln(X_i)$$

Supplementary Figure 9 | Minimum binary compound ΔH_f in meV/atom relative to pure elements, adapted from¹⁷.

	Al	V	Cr	Fe	Co	Ni
Al	0	-282	-138	-369	-629	-677
V	-282	0	-88	-176	-199	-250
Cr	-138	-88	0	-8	5	-30
Fe	-369	-176	-8	0	-60	-97
Co	-629	-199	5	-60	0	-21
Ni	-677	-250	-30	-97	-21	0

The simplest (and most calamitous) evidence against the “fast DFT” approach are the Al–V–Cr–Fe–Co–Ni and V–Cr–Fe–Co–Ni single phase HEAs produced by this work. In the DFT matrix, the Al–Ni binary enthalpy of -677 meV/atom would require an annealing temperature to exceed 4100°C (a nonsensical answer), and the V–Ni binary would require such a temperature to be above the alloys’ solidus in most cases. Even for the more approachable V–Cr–Fe–Co–Ni system (whose enthalpy need only be less than -250 meV/atom), an equiatomic set requires an annealing temp in excess of 1525°C, which is above the solidus temperature of most combinations of these elements in delineations of 5%.

Various combinations of these “impossible” HEAs have been verified experimentally as single phase solid solutions by other authors.^{21, 22, 23, 24} While these approaches might seem sensible in common HEA contexts (like that of Cr–Fe–Co–Ni), they incontrovertibly ignore higher dimensional phase complexities. A notable shortcoming likely comes from elements like aluminum acting as a stabilizer of crystal structures distinct from its primary unary structure,²² and also from the lack of any consideration of higher order mixing parameters like that of the Redlich-Kirsten model on which modern CALPHAD methods are based.²⁵

S7 THERMODYNAMIC DATABASES SUITABLE FOR HEAS

The Authors recommend investigating thermodynamic databases ahead of time in order to increase the reliability of chosen CALPHAD tools. [Supplementary Table 12](#) lists two of the premiere commercially available technologies which would be more than suitable for this type of project.

Supplementary Table 12 | List of ternary assessments for the Al–V–Cr–Fe–Co–Ni system for leading commercial CALPHAD software with publicly available packages.

<i>Software</i>	ThermoCalc	Pandat	<i>Software</i>	ThermoCalc	Pandat
<i>Database</i>	TCHEA6.1	PanHEA2022	<i>Database</i>	TCHEA6.1	PanHEA2022
<i>Date</i>	2023	2022	<i>Date</i>	2023	2022
<i>Al-V-Cr</i>	Yes	No	<i>V-Cr-Fe</i>	Yes	No
<i>Al-V-Fe</i>	No	Yes	<i>V-Cr-Co</i>	Yes	Yes
<i>Al-V-Co</i>	No	No	<i>V-Cr-Ni</i>	No	Yes
<i>Al-V-Ni</i>	No	Yes	<i>V-Fe-Co</i>	No	Yes
<i>Al-Cr-Fe</i>	Yes	Yes	<i>V-Fe-Ni</i>	Yes	Yes
<i>Al-Cr-Co</i>	Yes	Yes	<i>V-Co-Ni</i>	No	No
<i>Al-Cr-Ni</i>	Yes	Yes	<i>Cr-Fe-Co</i>	Yes	Yes
<i>Al-Fe-Co</i>	No	Yes	<i>Cr-Fe-Ni</i>	Yes	Yes
<i>Al-Fe-Ni</i>	Yes	Yes	<i>Cr-Co-Ni</i>	Yes	Yes
<i>Al-Co-Ni</i>	Yes	Yes	<i>Fe-Co-Ni</i>	Yes	Yes

The authors must note that while this method worked for the purposes of creating new alloys, the initial iteration was over-constrained. ThermoCalc sometimes retains floating point errors in its composition fractions and can incorrectly calculate a 100% FCC alloy to be all but one in 10^{15} parts FCC (0.99999 99999 99999 x...), which an equality constraint will filter out (this can be verified with the GUI for select compositions). A way to avoid this error is to apply inequalities even for binary decisions; constraining the system to FCC fractions > 0.999999 correctly identifies the 100% FCC materials and reduces the system to 2773 alloys, 1771 with low SFE and 1002 with high SFE. However, for the purposes of demonstrating the framework, the previous smaller sets were used.

S8 SFE Model

We created a new Gaussian Process Regressor (GPR) using 498 DFT-calculated compositions²⁶. Out of the well known Gaussian Process kernels, the Matern kernel produced the most consistent results with a total $R^2 = 0.939$ at a training size of 320 medoids. This GPR confirmed the GPR in the referenced SFE model within the main text²⁷. Both Gaussian Process and Support Vector Regressors achieved similar SFE root mean square errors (RMSE) of 22.6 mJ/m² and 24.8 mJ/m² respectively. GPR RMSE's were calculated using MatLab's Statistics and Machine Learning Toolbox.

References

1. Zarnetta R, Takahashi R, Young ML, Savan A, Furuya Y, Thienhaus S, et al. Identification of Quaternary Shape Memory Alloys with Near-Zero Thermal Hysteresis and Unprecedented Functional Stability. *Advanced Functional Materials*. 2010;20(12):1917-23.
2. Gu H, Bumke L, Chluba C, Quandt E, James RD. Phase engineering and supercompatibility of shape memory alloys. *Materials Today*. 2018;21(3):265-77.
3. OEIS Foundation Inc. (2022), The On-Line Encyclopedia of Integer Sequences, Published electronically at <https://oeis.org> 2022 [
4. Ghassemali E, Conway PLJ. High-Throughput CALPHAD: A Powerful Tool Towards Accelerated Metallurgy. *FRONTIERS IN MATERIALS*. 2022;9.
5. Spivak DI, editor *METRIC REALIZATION OF FUZZY SIMPLICIAL SETS* 2009.
6. McInnes L, Healy J, Melville J. *UMAP: Uniform Manifold Approximation and Projection for Dimension Reduction*. 2018.
7. Hume-Rothery Rules. *Van Nostrand's Scientific Encyclopedia*: John Wiley & Sons, Inc.; 2005.
8. Callister WD, Rethwisch DG. *Materials science and engineering : an introduction*. 10th edition. SI version. Global edition ed. Hoboken, NJ: Wiley; 2020.
9. Yang X, Zhang Y. Prediction of high-entropy stabilized solid-solution in multi-component alloys. *Materials Chemistry and Physics*. 2012;132(2):233-8.
10. Dayah M. Periodic Table - Ptable 1997 [Available from: <https://ptable.com>.
11. Takeuchi A, Inoue A. Classification of Bulk Metallic Glasses by Atomic Size Difference, Heat of Mixing and Period of Constituent Elements and Its Application to Characterization of the Main Alloying Element. *MATERIALS TRANSACTIONS*. 2005;46(12):2817-29.
12. Zhang RF, Zhang SH, He ZJ, Jing J, Sheng SH. Miedema Calculator: A thermodynamic platform for predicting formation enthalpies of alloys within framework of Miedema's Theory. *Computer Physics Communications*. 2016;209:58-69.
13. Gao MC, Alman DE. Searching for Next Single-Phase High-Entropy Alloy Compositions. *Entropy* [Internet]. 2013; 15(10):[4504-19 pp.].
14. Gao MC. *High-entropy alloys : fundamentals and applications*: Springer International Publishing; 2016.
15. Zhang Y, Zuo TT, Tang Z, Gao MC, Dahmen KA, Liaw PK, et al. Microstructures and properties of high-entropy alloys. *Progress in Materials Science*. 2014;61:1-93.
16. Zhao YJ, Qiao JW, Ma SG, Gao MC, Yang HJ, Chen MW, et al. A hexagonal close-packed high-entropy alloy: The effect of entropy. *Materials & Design*. 2016;96:10-5.
17. Troparevsky MC, Morris JR, Kent PRC, Lupini AR, Stocks GM. Criteria for Predicting the Formation of Single-Phase High-Entropy Alloys. *Physical Review X*. 2015;5(1).
18. Curtarolo S, Hart GLW, Nardelli MB, Mingo N, Sanvito S, Levy O. The high-throughput highway to computational materials design. *Nature Materials*. 2013;12(3):191-201.
19. Curtarolo S, Setyawan W, Hart GLW, Jahnatek M, Chepulskii RV, Taylor RH, et al. AFLOW: An automatic framework for high-throughput materials discovery. *Computational Materials Science*. 2012;58:218-26.
20. Manzoni A, Daoud H, Völkl R, Glatzel U, Wanderka N. Phase separation in equiatomic AlCoCrFeNi high-entropy alloy. *Ultramicroscopy*. 2013;132:212-5.
21. Li J, Lu K, Zhao X, Ma X, Li F, Pan H, et al. A superior strength-ductility synergy of Al_{0.1}CrFeCoNi high-entropy alloy with fully recrystallized ultrafine grains and annealing twins. *Journal of Materials Science & Technology*. 2022;131:185-94.
22. Liu T, Chen R, Gao X, Fang H, Qin G, Su Y, et al. Formation of hypoeutectic structure and strengthening mechanism of Co₄Cr_{1.5}Fe_{1.5}Ni₅ high entropy alloy alloyed by Al. *Journal of Alloys and Compounds*. 2022;923:166372.
23. Wang W-R, Wang W-L, Wang S-C, Tsai Y-C, Lai C-H, Yeh J-W. Effects of Al addition on the microstructure and mechanical property of Al_xCoCrFeNi high-entropy alloys. *Intermetallics*. 2012;26:44-51.
24. Zhang Y, Zhou YJ, Lin JP, Chen GL, Liaw PK. Solid-Solution Phase Formation Rules for Multi-component Alloys. *Advanced Engineering Materials*. 2008;10(6):534-8.
25. Redlich O, Kister AT. Algebraic Representation of Thermodynamic Properties and the Classification of Solutions. *Industrial & Engineering Chemistry*. 1948;40(2):345-8.
26. Oh HS, Kim SJ, Odbadrakh K, Ha Ryu W, Yoon KN, Mu S, et al. Engineering atomic-level complexity in high-entropy and complex concentrated alloys. *Nat Commun*. 2019;10.
27. Khan TZ, Kirk T, Vazquez G, Singh P, Smirnov AV, Johnson DD, et al. Towards stacking fault energy engineering in FCC high entropy alloys. *Acta Materialia*. 2022;224:117472.